

Carnegie Supernova Project: The First Homogeneous Sample of “Super-Chandrasekhar Mass”/2003fg-like Type Ia Supernova

C. ASHALL,¹ J. LU,² E. Y. HSIAO,² P. HOEFLICH,² M. M. PHILLIPS,³ L. GALBANY,⁴ C. R. BURNS,⁵ C. CONTRERAS,³
K. KRISCIUNAS,⁶ N. MORRELL,³ M. D. STRITZINGER,⁷ N. B. SUNTZEFF,⁶ F. TADDIA,⁷ J. ANAIS,³ E. BARON,^{8,9}
P. J. BROWN,¹⁰ L. BUSTA,³ A. CAMPILLAY,¹¹ S. CASTELLÓN,³ C. CORCO,^{3,12} S. DAVIS,¹³ G. FOLATELLI,¹⁴ F. FÖRSTER,^{15,16}
W. L. FREEDMAN,¹⁷ C. GONZALÉZ,³ M. HAMUY,¹⁸ S. HOLMBO,⁷ R. P. KIRSHNER,^{19,20} S. KUMAR,²¹ G. H. MARION,²²
P. MAZZALI,²³ T. MOROKUMA,²⁴ P. E. NUGENT,^{25,26} S. E. PERSSON,⁵ A. L. PIRO,⁵ M. ROTH,^{3,27} F. SALGADO,³
D. J. SAND,²⁸ J. SERON,^{3,29} M. SHAHBANDEH,² AND B. J. SHAPPEE¹

¹*Institute for Astronomy, University of Hawaii, 2680 Woodlawn Drive, Honolulu, HI 96822, USA*

²*Department of Physics, Florida State University, 77 Chieftan Way, Tallahassee, FL 32306, USA*

³*Carnegie Observatories, Las Campanas Observatory, Casilla 601, La Serena, Chile*

⁴*Institute of Space Sciences (ICE, CSIC), Campus UAB, Carrer de Can Magrans, s/n, E-08193 Barcelona, Spain.*

⁵*The Observatories of the Carnegie Institution for Science, 813 Santa Barbara Street, Pasadena, CA 91101, USA*

⁶*George P. and Cynthia Woods Mitchell Institute for Fundamental Physics & Astronomy, Texas A&M University, Department of Physics and Astronomy, 4242 TAMU, College Station, TX 77843*

⁷*Department of Physics and Astronomy, Aarhus University, Ny Munkegade 120, DK-8000 Aarhus C, Denmark*

⁸*Homer L. Dodge Department of Physics and Astronomy, University of Oklahoma, 440 W. Brooks, Rm 100, Norman, OK 73019-2061, USA*

⁹*Hamburger Sternwarte, Gojenbergsweg 112, D-21029 Hamburg, Germany*

¹⁰*George P. and Cynthia Woods Mitchell Institute for Fundamental Physics and Astronomy, Department of Physics and Astronomy, Texas A&M University, College Station, TX 77843, USA*

¹¹*Departamento de Física, Universidad de La Serena, Cisternas 1200, La Serena, Chile*

¹²*SOAR Telescope, Casilla 603, La Serena, Chile*

¹³*Department of Physics and astronomy, University of California, 1 Shields Avenue, Davis, CA 95616-5270, USA*

¹⁴*Facultad de Ciencias Astronómicas y Geofísicas, Universidad Nacional de La Plata, Instituto de Astrofísica de La Plata (IALP), CONICET, Paseo del Bosque S/N, B1900FWA La Plata, Argentina*

¹⁵*Millennium Institute of Astrophysics, Casilla 36-D, 7591245, Santiago, Chile*

¹⁶*Departamento de Astronomía, Universidad de Chile, Casilla 36-D, Santiago, Chile*

¹⁷*Department of Astronomy and Astrophysics, University of Chicago, 5640 S. Ellis Avenue, Chicago, IL 60637, USA*

¹⁸*Universidad de Chile, Departamento de Astronomía, Casilla 36-D, Santiago, Chile*

¹⁹*Gordon and Betty Moore Foundation, 1661 Page Mill Road, Palo Alto, CA 94304, USA*

²⁰*Harvard-Smithsonian Center for Astrophysics, 60 Garden Street, Cambridge, MA 02138, USA*

²¹*Department of Physics, Florida State University, Tallahassee, FL 32306, USA*

²²*University of Texas at Austin, 1 University Station C1400, Austin, TX 78712-0259, USA*

²³*Astrophysics Research Institute, Liverpool John Moores University, IC2, Liverpool Science Park, 146 Brownlow Hill, Liverpool L3 5RF, UK*

²⁴*Institute of Astronomy, Graduate School of Science, The University of Tokyo, 2-21-1 Osawa, Mitaka, Tokyo 181-0015, Japan*

²⁵*Lawrence Berkeley National Laboratory, Department of Physics, 1 Cyclotron Road, Berkeley, CA 94720, USA*

²⁶*Astronomy Department, University of California at Berkeley, Berkeley, CA 94720, USA*

²⁷*GMTO Corporation, Presidente Riesco 5335, Of. 501, Nueva Las Condes, Santiago*

²⁸*Steward Observatory, University of Arizona, 933 North Cherry Avenue, Rm. N204, Tucson, AZ 85721-0065, USA*

²⁹*Cerro Tololo Inter-American Observatory, Casilla 603, La Serena, Chile*

(Received September 2, 2021; Revised; Accepted)

Submitted to ApJ

ABSTRACT

We present a multi-wavelength photometric and spectroscopic analysis of thirteen “Super-Chandrasekhar Mass”/2003fg-like type Ia Supernova (SNe Ia). Nine of these objects were observed by the Carnegie Supernova Project. 2003fg-like SNe have slowly declining light curves ($\Delta m_{15}(B) < 1.3$ mag), and peak absolute B -band magnitudes between $-19 < M_B < -21$ mag. Many 2003fg-like SNe are located in the same part of the luminosity width relation as normal SNe Ia. In the optical B and V bands, 2003fg-like SNe look like normal SNe Ia, but at redder wavelengths they diverge. Unlike other luminous SNe Ia, 2003fg-like SNe generally have only one i -band maximum which peaks after the epoch of B -band maximum, while their NIR light curve rise times can be $\gtrsim 40$ days longer than those of normal SNe Ia. They are also at least one magnitude brighter in the NIR bands than normal SNe Ia, peaking above $M_H < -19$ mag, and generally have negative Hubble residuals, which may be the cause of some systematics in dark energy experiments. Spectroscopically, 2003fg-like SNe exhibit peculiarities such as unburnt carbon well past maximum light, a large spread (8000–12000 km s⁻¹) in Si II $\lambda 6355$ velocities at maximum light with no rapid early velocity decline, and no clear H -band break at +10 d, e. We find that SNe with a larger pseudo equivalent width of C II at maximum light have lower Si II $\lambda 6355$ velocities and slower declining light curves. There are also multiple factors that contribute to the peak luminosity of 2003fg-like SNe. The explosion of a C-O degenerate core inside a carbon-rich envelope is consistent with these observations. Such a configuration may come from the core degenerate scenario.

Keywords: supernovae: general

1. INTRODUCTION

Type Ia supernovae (SNe Ia) originate from the thermonuclear explosion of at least one C-O White Dwarf (WD) in a binary system (e.g., Whelan & Iben 1973; Livne 1990; Iben & Tutukov 1984; Hoefflich & Khokhlov 1996). These luminous events follow empirical observational relationships which are fundamental for the use of SNe Ia as extra galactic distance indicators (Pskovskii 1984; Phillips 1993; Phillips et al. 1999). This led to the discovery of the accelerating expansion of the cosmos, or dark energy (e.g., Riess et al. 1998; Perlmutter et al. 1999).

To date, there have been many sub-types of SNe Ia discovered including: 1991bg-like SNe (e.g., Filippenko et al. 1992a; Leibundgut et al. 1993), transitional SNe (e.g., Hsiao et al. 2015; Gall et al. 2018), 2002cx-like SNe (e.g., Li et al. 2003; Foley et al. 2013), 2002es-like SNe (e.g., Ganeshalingam et al. 2012), 1991T-like SNe (e.g., Filippenko et al. 1992b; Phillips et al. 1992) and 2003fg-like SNe (e.g., Howell et al. 2006; Hicken et al. 2007). 2003fg-like SNe, which are also known as “super-Chandrasekhar-mass” SNe Ia, are among the most rare sub-type of SNe Ia. It was previously thought that all 2003fg-like SNe were over-luminous and require more ⁵⁶Ni to power the light curve than could be produced in a detonation of a non-rotating Chandrasekhar-mass (M_{Ch}) C-O WD (Howell et al. 2006; Hicken et al. 2007). Hence, they were named “super-Chandrasekhar mass”. However, it has since become evident that not all 2003fg-like SNe are over-luminous and their proper-

ties are more diverse (e.g., Taubenberger et al. 2019; Lu et al. 2021). Therefore, in this work, we follow the convention of naming the sub-type after the first SN discovered in the group, SN 2003fg (Howell et al. 2006).

There have only been a handful of 2003fg-like SNe discovered and their observational traits are varied (Howell et al. 2006; Hicken et al. 2007; Yamanaka et al. 2009; Scalzo et al. 2010; Yuan et al. 2010; Silverman et al. 2011; Taubenberger et al. 2011; Chakradhari et al. 2014; Taubenberger et al. 2019; Hsiao et al. 2020; Lu et al. 2021). They do, however, share a few characteristics: They generally have broad light curves, slow expansion velocity gradient before maximum light, and a very strong $\lambda 6580$ C II absorption feature which lasts well past B -band maximum. They also peak in the i -band well after the time of B -band maximum (Ashall et al. 2020). Furthermore, 2003fg-like SNe do not show a distinct H -band break at +10 d past B -band maximum which is seen in normal SNe Ia (Taubenberger et al. 2011; Hsiao et al. 2019; Lu et al. 2021). This H -band break is directly linked to the distribution and bulk of ⁵⁶Ni in the explosion (Wheeler et al. 1998). SN 2007if and SN 2009dc show low continuum polarizations which suggest spherical explosions (Tanaka et al. 2010; Cikota et al. 2019). SN 2012dn and LSQ14fmg show evidence of dense circumstellar medium (CSM) (Nagao et al. 2017; Hsiao et al. 2020). The majority of 2003fg-like SNe occur in low metallicity, low surface brightness galaxies with high specific star formation rates (Childress et al.

2011; Hsiao et al. 2020; Lu et al. 2021; Galbany et al. 2021).

There are several theoretical models that have been proposed for 2003fg-like SNe. An early suggestion is the violent merger of two WDs that exceed the M_{ch} (Howell et al. 2006; Scalzo et al. 2010). Alternatively, others have suggested these bright SNe experience interaction with dense CSM (Hachinger et al. 2012; Noebauer et al. 2016). This is also referred to as an envelope model (Hoeftlich & Khokhlov 1996). Such an explosion may occur from the explosion of a degenerate core of an Asymptotic giant branch (AGB) star in the core degenerate scenario (Kashi & Soker 2011; Hsiao et al. 2020; Lu et al. 2021) or from the disruption of a C-O WD with surrounding circumstellar dust (Nagao et al. 2017, 2018). Finally, the explosion of a C-O WD which exceeds the classical non-rotating M_{ch} limit due to rapid rotation or high magnetic fields may also be a viable model (Yoon & Langer 2005; Das & Mukhopadhyay 2013). The current dataset of 2003fg-like SNe is sparse, and it has not been possible to disentangle the effects predicted by these scenarios.

The *Carnegie Supernova project-I & II* (CSP-I & II) ran two observing campaigns between 2004 and 2015, during which we obtained optical and NIR spectra and photometry of over 300 SNe Ia (Krisciunas et al. 2017; Phillips et al. 2019; Hsiao et al. 2019). Nine 2003fg-like SNe were followed in these two campaigns. In this work, we combine this data set with data from the literature to produce and analyze the first statistical and homogeneous sample 2003fg-like SNe. In Section 2 we present the observational sample, followed by the data reduction in Section 3. Host galaxy extinction is discussed in Section 4. Section 5 presents the photometric observations, followed by the spectroscopic observations in Section 6. Important correlations and their implications are discussed in Section 7. Finally the discussion of possible explosion models is given in Section 8, followed by the conclusions in Section 9.

2. SAMPLE CHARACTERISTICS

The vast majority of the 2003fg-like SNe followed by CSP were observed during CSP-II (7 out of 9). This reflects one of the main differences between the CSP-I and CSP-II campaigns: while nearly 90% of the SNe Ia followed up by CSP-I came from targeted searches, 83% of those followed up by CSP-II came from untargeted searches. As 2003fg-like SNe preferentially explode in low-luminosity hosts, untargeted surveys have the advantage in detecting them. While we strove for a complete and unbiased sample in CSP-II, the strategy also contributes to our success at following up on a statisti-

cally significant and uniform sample of 2003fg-like SNe, the only sample of its kind. Furthermore, the sample optical light curves are obtained with nearly nightly cadence and are placed on a single well-understood photometric system of the Swope Telescope. All of the 2003fg-like SNe observed by CSP-II came from untargeted searches. Only 3 (SNe 2006gz, 2009dc, and 2012dn) out of the 13 2003fg-like SNe presented here were discovered by targeted searches. The discovery information on the objects not previously published can be seen in Appendix A.1.

2003fg-like SNe are generally characterized by:

- ★ A primary i -band maximum after that of the B -band maximum
- ★ A lack of H -band break at +10 d in the NIR spectra
- ★ A low ionization state in nebular phase spectra
 - A broad light curve
 - A strong C II $\lambda\lambda 6578, 6582$ feature past maximum light
 - A lack of or weak i -band secondary maximum
 - Low ejecta velocity gradients before maximum light
 - A lack of Ti II in the maximum light spectra

However, not all of these features are observed in every 2003fg-like SN, and only the timing of the i -band primary, the lack of an H -band break, and the low ionization nebular phase appear to be ubiquitous (see e.g., Howell et al. 2006; Silverman et al. 2011; Taubenberger et al. 2011, 2019; Chen et al. 2019; Hsiao et al. 2019; Ashall et al. 2020; Lu et al. 2021).

In this work the 2003fg-like SNe were identified in the CSP-I and CSP-II through photometric criteria. As mentioned previously, 2003fg-like SNe have distinct photometric properties from the normal population as well as other peculiar sub-types (González-Gaitán et al. 2014). Here we adopt the method of Ashall et al. (2020) to identify 2003fg-like SNe: For an object to be chosen for the sample, it must have its i -band primary maximum occurring after that in B band. Furthermore, the object must have slowly declining light curves as indicated by $s_{BV} \gtrsim 0.8$ or $\Delta m_{15}(B) \lesssim 1.3$ mag¹.

These photometric selection criteria are then used in conjunction with the examination of its optical spectrum

¹ See section 5.2 for the definition of s_{BV} and $\Delta m_{15}(B)$.

near maximum to look for the identifying properties of 2003fg-like SNe described above. The spectroscopic criteria eliminate the peculiar SN 2006bt, as it contains Ti II features. Note that using spectra alone can lead to misleading results, such as those of SN 2011hr (Zhang et al. 2016) and LSQ12gdj (Scalzo et al. 2014). Note that CSS140126 is a border-line case between a 1991T-like and a 2003fg-like SNe, it has only one low S/N optical spectrum which is featureless, a primary i -band maximum which peaks after that of B band, but displays a secondary i -band maximum. We chose to keep it in the sample, however due to poor spectral temporal coverage it is difficult to ascertain if it is a true 2003fg-like SN. Nine SNe in the CSP samples and a further four in the literature were found to meet these criteria.

Table 1 contains the basic information of all of the SNe used in this analysis, and Table 2 summarizes their photometric properties. For ten objects z_{helio} was determined using integral field spectroscopy (IFS) data which will be presented in (Galbany et al. 2021). For the other objects z_{helio} was determined from a spectrum of the host galaxy, or, in the case of previously published 2003fg-like SNe objects, it was taken from the literature. In Fig. 1, the sample characteristics are compared to that of the ‘‘Cosmology’’ SN Ia sample of CSP-II (Phillips et al. 2019), as 96% of the SNe were discovered by untargeted searches. The majority of the objects from the sample are in the Hubble flow, similar to the CSP-II Cosmology sample. As our selection criteria dictate, the 2003fg-like SNe are slow decliners as indicated by s_{BV} and $\Delta m_{15}(B)$. However, it should be noted that there is a wide range of light-curve properties that overlap with those of the normal populations.

3. DATA REDUCTION

3.1. Photometry

Optical $uBVgri$ -band imaging was obtained for nine 2003fg-like SNe using SITE-3 and e2v on the 1-m Swope telescope at Las Campanas Observatory (LCO). For a sub-sample of these, NIR YJH -band imaging was also acquired using NIR imager called RetroCam which was installed on the Swope telescope during CSP-I and the 2.5-m du Pont telescope during CSP-II. All of the photometry presented here is on the well-understood CSP natural system. This allows for systematic differences between SNe to be examined. The reduction and calibration procedures are described in Krisciunas et al. (2017) and Phillips et al. (2019), and the final light

curves can be found online². The light curves of four of the nine SNe have been previously published by the CSP: SN 2007if and SN 2009dc (Krisciunas et al. 2017), LSQ14fmg (Hsiao et al. 2020), and ASASSN-15hy (Lu et al. 2021). Finder charts of the remaining five 2003fg-like SNe are presented in Fig. 2, and the light curves of all the SNe are presented in the natural system in Fig. 3. These light curves are tabulated in Appendix A.2.

Data from five 2003fg-like SNe that have been published by other groups (SN 2003fg; Howell et al. 2006, SN 2006gz; Hicken et al. 2007 SN 2009dc; Yamanaka et al. 2009; Tanaka et al. 2010; Silverman et al. 2011; Taubenberger et al. 2011, SN 2012dn; Chakradhari et al. 2014; Parrent et al. 2016; Taubenberger et al. 2019, and ASASSN-15pz; Chen et al. 2019) are also included in the sample. In the $BVgri$ bands, where possible, S-corrections were applied to transform the photometry to the CSP natural system. Swift Ultraviolet/Optical Telescope (UVOT) data of SN 2015M was also obtained from the Supernova Archive (SOUSA; Brown et al. 2014a) via the Swift Supernova website.³

K-corrections were computed for $BVgri$ light curves using the same method presented in Appendix B of Lu et al. (2021). In short, the spectral series of SN 2009dc, SN 2012dn, ASASSN-15hy, and the Hsiao template were all used independently as the SED to compute the corrections. The SEDs were mangled to match the interpolated observed photometric colors. A comparison was made between the K-correction values between the four SED template spectral series and those computed with the actual observed spectra of the SNe. The template with the smallest average residual K-correction compared to the observed spectra was then selected for each SN. This was done because most of the SNe did not have adequate spectral coverage to compute K-corrections directly from the observed spectra. The K-correction process was carried out individually for each SN. As discussed in Lu et al. (2021), the average K-correction uncertainty obtained with this method is smaller than 0.01 mag, which is consistent with the values obtained for normal SNe Ia from Hsiao et al. (2007). Due to the lack of spectral data in the UV and NIR, and hence the ability to understand the SED, no S or K-corrections were applied in these regions.

3.2. Spectra

Optical and NIR spectra were obtained of nine 2003fg-like SNe by the CSP I & II. Twenty-four optical and six

² CSP data products.

³ <https://pbrown801.github.io/SOUSA/>

Table 1. The properties of the SNe in the sample.

SN	z_{helio}	RA	DEC	μ^a Mag	$E(B - V)_{MW}$ Mag	Discoverer
2003fg	0.2440	14:16:18.8	+52:14:53.66	40.37 ± 0.01	0.011	Howell et al. (2006)
2006gz	0.0237	18:10:26.3	+30:59:44.40	34.95 ± 0.09	0.055	Puckett & Pelloni, (2006)
2012dn	0.0100	20:23:36.3	-28:16:43.40	33.28 ± 0.21^b	0.052	Bock et al. (2012)
ASASSN-15pz	0.0148	03:08:48.4	+35:13:50.89	33.89 ± 0.14	0.015	Brimacombe et al. (2015)
2007if ^c	0.0742	01:10:51.4	+15:27:39.90	37.51 ± 0.03	0.072	Akerlof et al. (2007)
2009dc ^c	0.0214	15:51:12.1	+25:42:28.50	34.79 ± 0.09	0.060	Puckett et al. (2009)
LSQ12gpw ^c	0.0506	03:12:58.2	-11:42:40.13	36.65 ± 0.04	0.062	Baltay et al. (2013a)
2013ao ^c	0.0435	11:44:44.7	-20:31:41.10	36.39 ± 0.04	0.034	Drake et al. (2013a)
CSS140126 ^{c d}	0.0772	12:03:06.9	-01:01:31.70	37.67 ± 0.03	0.021	Drake et al. (2009)
CSS140501 ^{c e}	0.0797	17:04:13.7	+17:48:39.40	37.74 ± 0.03	0.066	Drake et al. (2009)
LSQ14fmg ^c	0.0649	22:16:46.1	+15:21:14.13	37.24 ± 0.03	0.046	Baltay et al. (2013a)
2015M ^c	0.0231	13:00:32.3	+27:58:41.00	35.04 ± 0.08	0.009	Morokuma et al. (2015)
ASASSN-15hy ^c	0.0185	20:10:02.4	-00:44:21.31	34.33 ± 0.11	0.130	Holoien et al. (2015)

^aCorrected to the CMB rest frame and calculated using $H_0=73 \text{ km s}^{-1} \text{ Mpc}^{-1}$, $\Omega_m=0.27$ and $\Omega_\Lambda=0.73$, which is used throughout this work.

^bCorrected for the infall towards the Virgo cluster and the Great Attractor (recession velocity =3300km s⁻¹; Mould et al. 2000).

^cSN observed by CSP.

^dFor convenience we shorten CSS140126:120307-010132 to CSS140126.

^eFor convenience we shorten CSS140501-170414+174839 to CSS140501.

NIR spectra are presented here for the first time, which are logged in Appendix A.2.

The majority of these optical spectra were acquired at LCO using B&C on the 2.5-m du Pont telescope and LDSS3 and IMACS on the 6.5-m Magellan Baade and Clay Telescopes. Additional spectra were obtained with the ALFOSC on the Nordic Optical Telescope (NOT) at La Palma, EFOSC2 on the New Technology Telescope (NTT) at La Silla, and RSS on the Southern African Large Telescope (SALT) at the South African Astronomical Observatory. The spectra were reduced using the standard IRAF⁴ packages using the method as described in Hamuy et al. (2006) and Folatelli et al. (2013).

All the NIR spectra were observed with the Folded-port InfraRed Echellette (FIRE; Simcoe et al. 2013). The details in observing set up and data reduction are outlined by Hsiao et al. (2019). Along with six NIR spec-

tra of ASASSN-15hy (Lu et al. 2021), we have tripled the size of the sample of 2003fg-like SNe NIR spectra, as the previous sample includes only spectra of SN 2009dc (Taubenberger et al. 2011, 2013b).

Plots of the previously unpublished CSP spectra of SN 2007if, SN 2009dc, LSQ12gpw, SN 2013ao, CSS140126, CSS140501, and SN 2015M are presented in Fig. 4 and Fig. 5. All of the spectra for analysis have been made available at the CSP website⁵.

4. EXTINCTION

Throughout this work, the dust map of Schlafly & Finkbeiner (2011) was used to correct for foreground Milky Way (MW) extinction. However, values of the host galaxy extinction of 2003fg-like SNe are still very uncertain due to the fact that their intrinsic brightness and colors are not yet fully understood.

Two methods were adopted to estimate the host extinction for the 2003fg-like SNe: i) the equivalent width (EW) of the host-galaxy Na I D feature and ii) the

⁴ The Image Reduction and Analysis Facility (IRAF) is distributed by the National Optical Astronomy Observatory, which is operated by the Association of Universities for Research in Astronomy, Inc., under cooperative agreement with the National Science Foundation.

⁵ CSP data products.

Table 2. The basic light curve parameters of the 2003fg-like SNe. All parameters were obtained from direct measurements to the Gaussian process interpolations to the data. It should be noted that the t_{max}^{i-B} here has not been K-corrected. These values have been corrected for foreground but not host galaxy extinction.

SN	$T(B)_{max}$	B_{max}	$\Delta m_{15}(B)$	s_{BV}	$(B - V)_{B_{max}}$	t_{max}^{i-B}
	Days	Mag	Mag		Mag	Days
2003fg	2452760.18 ± 0.87
2006gz	2454021.84 ± 0.10	15.86 ± 0.06	0.84 ± 0.02	1.37 ± 0.03	0.03 ± 0.02	4.60 ± 1.65
2012dn	2456132.63 ± 0.98	14.16 ± 0.03	0.87 ± 0.03	1.25 ± 0.15	0.02 ± 0.03	2.04 ± 0.61
ASASSN-15pz	2457307.47 ± 0.93	14.18 ± 0.03	0.67 ± 0.09	1.37 ± 0.09	-0.02 ± 0.02	0.04 ± 0.81
2007if	2454349.97 ± 1.09	17.55 ± 0.02	0.88 ± 0.09	1.26 ± 0.15	0.01 ± 0.03	3.03 ± 3.24
2009dc	2454947.07 ± 0.60	15.09 ± 0.02	0.70 ± 0.05	1.29 ± 0.07	-0.03 ± 0.01	2.52 ± 0.34
LSQ12gpw	2456269.75 ± 0.46	17.35 ± 0.01	0.70 ± 0.03	...	0.01 ± 0.01	...
2013ao	2456362.53 ± 0.26	16.87 ± 0.01	0.99 ± 0.03	1.02 ± 0.13	0.10 ± 0.01	1.80 ± 0.26
CSS140126	2456668.48 ± 0.41	18.23 ± 0.01	0.73 ± 0.05	...	-0.06 ± 0.01	3.97 ± 0.73
CSS140501	2456787.70 ± 1.60	18.09 ± 0.04	1.05 ± 0.18	...	0.03 ± 0.02	2.58 ± 2.85
LSQ14fmg	2456939.24 ± 0.72	17.35 ± 0.01	1.04 ± 0.09	1.20 ± 0.08	0.09 ± 0.01	1.51 ± 1.05
2015M	2457169.00 ± 0.82	15.54 ± 0.03	0.82 ± 0.04	...	0.14 ± 0.01	1.85 ± 2.22
ASASSN-15hy	2457151.63 ± 0.40	15.19 ± 0.01	0.73 ± 0.03	1.24 ± 0.18	0.19 ± 0.01	7.28 ± 0.47

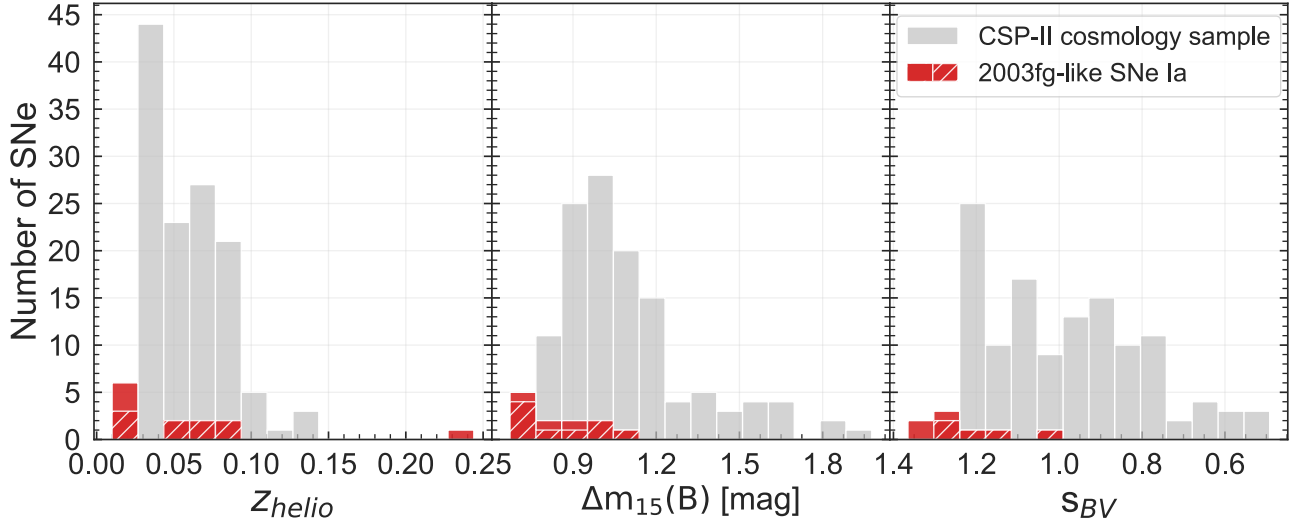


Figure 1. Histograms of z_{helio} (left panel), $\Delta m_{15}(B)$ (middle panel) and s_{BV} (right panel) of the 2003fg-like SNe sample compared to the CSP-II SNe Ia cosmology samples from Phillips et al. (2019). Nine 2003fg-like SNe followed up by CSP (including CSP-I and CSP-II) are marked with shaded red bars, and four not followed by CSP are stacked on top with non-stripped red bars. The SNe Ia from Phillips et al. (2019) are the gray shaded bars.

Balmer decrements of the host galaxy lines at the SN location using integral field spectroscopy (IFS) data from Galbany et al. (2021). Both of these techniques suffer from shortcomings, which we discuss below. It is established that if a SN has a Na I D feature it may have some host galaxy extinction, and in the Milky Way there is a well-known correlation between the A_V and the EW of Na I D (e.g., see Pozananski et al. 2012 and ref-

erences therein). However, the scatter in this correlation is $\pm 68\%$ and a significant fraction of SNe Ia display anomalously high Na I D EWs in comparison with the A_V values derived from their colors (Phillips et al. 2013). Furthermore, most of the spectra we analyze in this work are of low resolution, making it difficult to detect a weak Na I D feature.

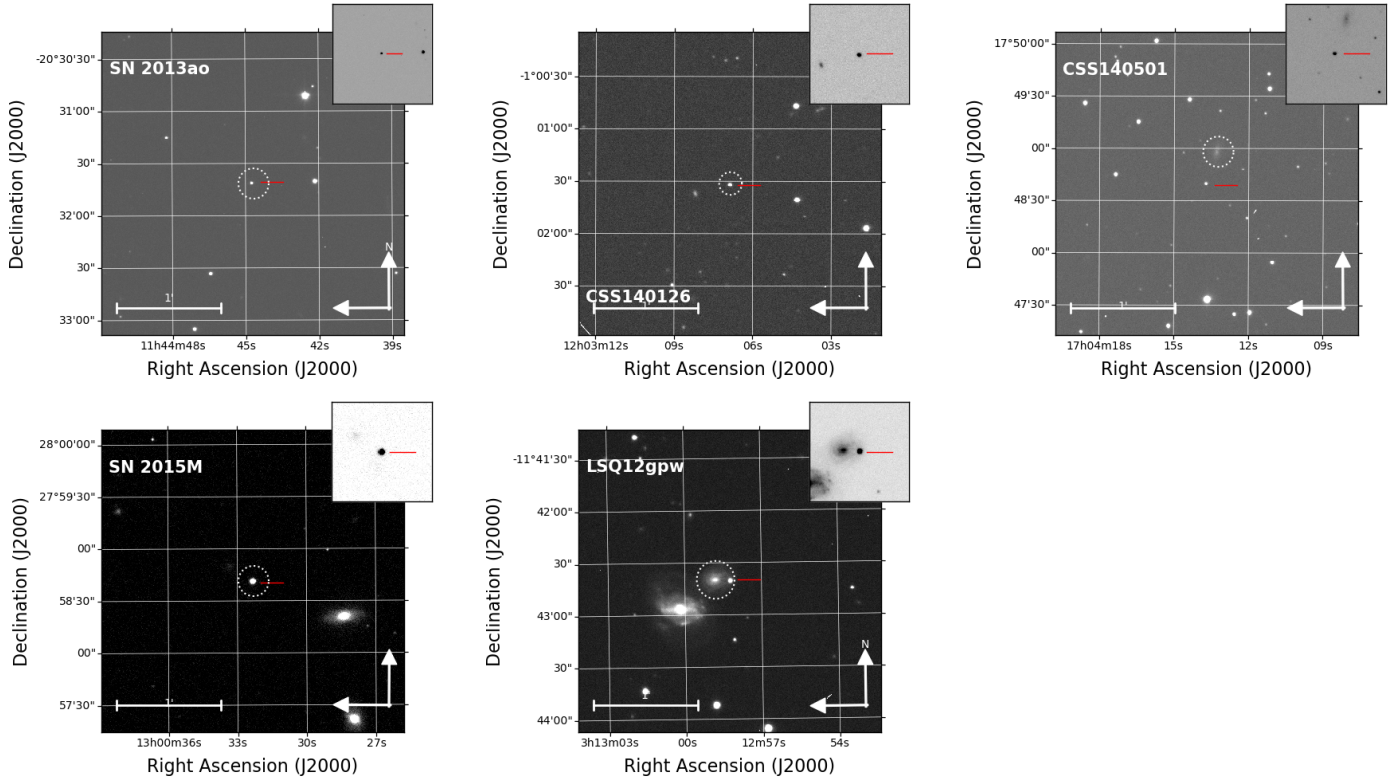


Figure 2. The r -band finding charts of the five 2003fg-like SNe observed by CSP-II. The plots are produced with Swope eV2 images. An inset of the exact SN location is provided in the top right section of each panel.

If no Na I D feature can be detected in the observed spectrum we simulate an upper limit on how much Na I D absorption could be hidden in the data. This was done by using the highest resolution observed spectrum for each SN. An idealized spectrum with infinite resolution was created by smoothing the observed spectrum via a Gaussian filter. An artificial absorption line with various widths and depths simulating the Na I D feature was then added at the host redshift. This idealized spectrum was degraded to the resolution of the observations. The spectrum was re-sampled at the same wavelengths as the observed spectrum. Finally, random noise was added using the flux uncertainty measured from the observed spectrum. The EW of the Na I D feature was measured in the idealized spectrum and the low-resolution spectrum. The strength of the absorption was decreased until the EW of the low-resolution spectrum equals the EW uncertainty. At this point, the EW of the idealized spectrum is taken as the detection limit. The results are presented in Table 3. The Na I D pEW was then converted to an $E(B - V)$ value using the relation from Poznanski et al. (2012), with a 68% uncertainty as per Phillips et al. (2013).

The second method to determine host-galaxy extinction is using the host-galaxy emission lines at the location of the SN. This has been obtained for ten of the thir-

teen SNe we analyzed in this work (see Galbany et al. 2021). The IFS data, which is presented in Galbany et al. (2021), can be used to determine these values. However, this is highly uncertain as it assumes a constant temperature of the gas, and considers the whole column density at the location of the SN, not just in front of it. Only LSQ12gpw has a significant extinction detected at its location using this method.

Note that the host extinction may be estimated for normal SNe Ia using the Lira Law (Lira et al. 1998; Phillips et al. 1999), and this was attempted by Chen et al. (2019) for SN 2009dc and ASASSN-15pz. The host galaxy extinction of SN 2009dc has always been uncertain. Chen et al. (2019) found that SN 2009dc, which has a large Na I D host galaxy feature, had the same $B - V$ color slope as ASASSN-15pz. It was then presumed that ASASSN-15pz could be used as an “unreddened” comparison SN. The magnitude offset between the two SNe at the late-time decline was assumed to be caused by extinction. However, there is no evidence for 2003fg-like SNe following a form of Lira Law, and Hicken et al. (2007) claimed the host color excess derived from Lira relation is most likely not appropriate for 2003fg-like SNe. Therefore, we choose not to use this relation. Furthermore, Lu et al. (2021) found that 2003fg-like SNe can look similar after B -band maximum

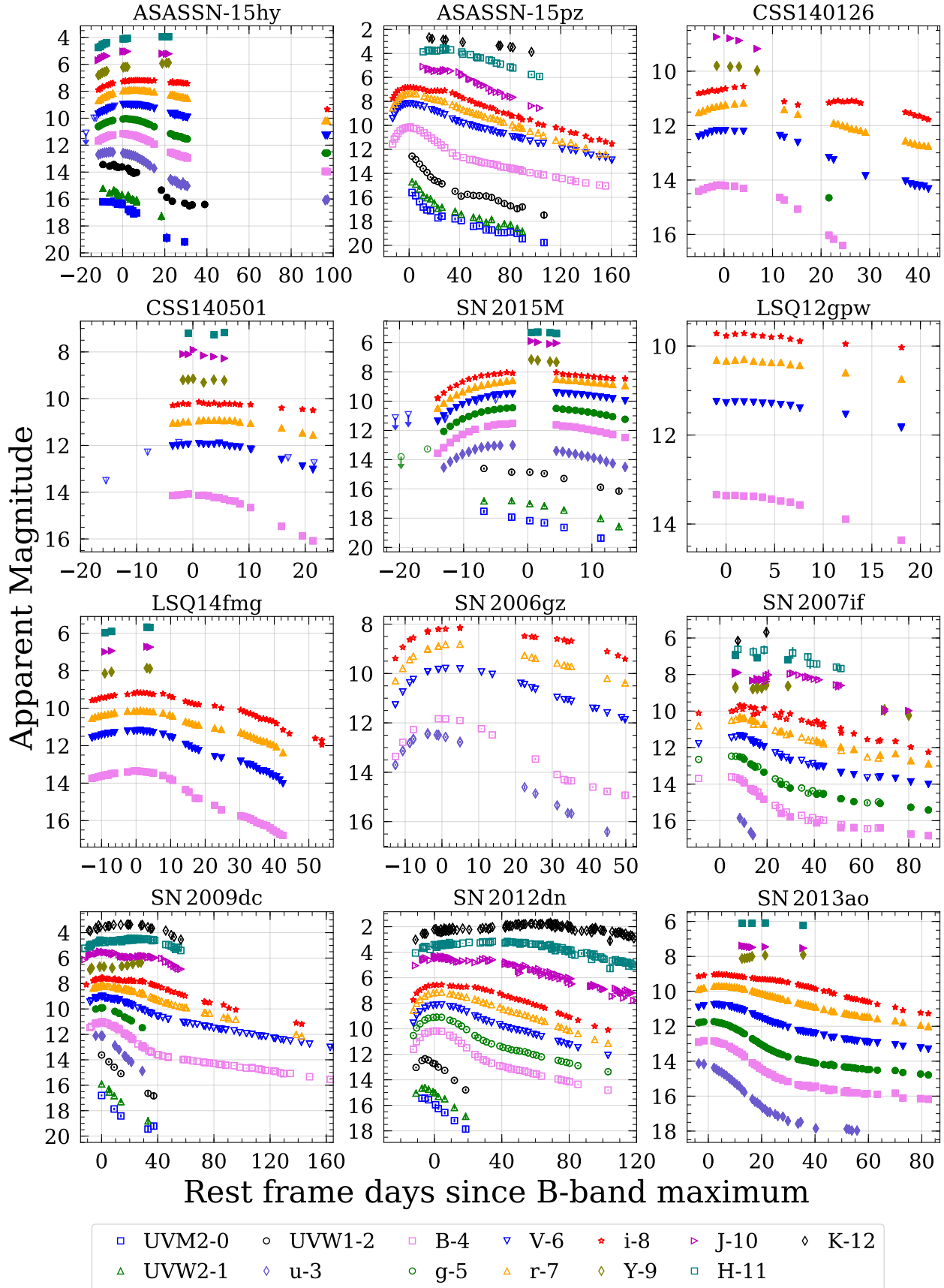


Figure 3. Rest-frame UV to NIR photometry of all 2003fg-like SNe in the sample. The photometry in this plot has not been K-corrected or corrected for host galaxy extinction, but have been corrected for foreground extinction. Filled symbols are photometric measurements computed from Swope or du Pont telescope images and are in the CSP natural system. The open symbols are from other sources. SN 2003fg has been excluded from the plot due to poor photometric coverage. Individual light curve plots of these SN can be found in Appendix A.2

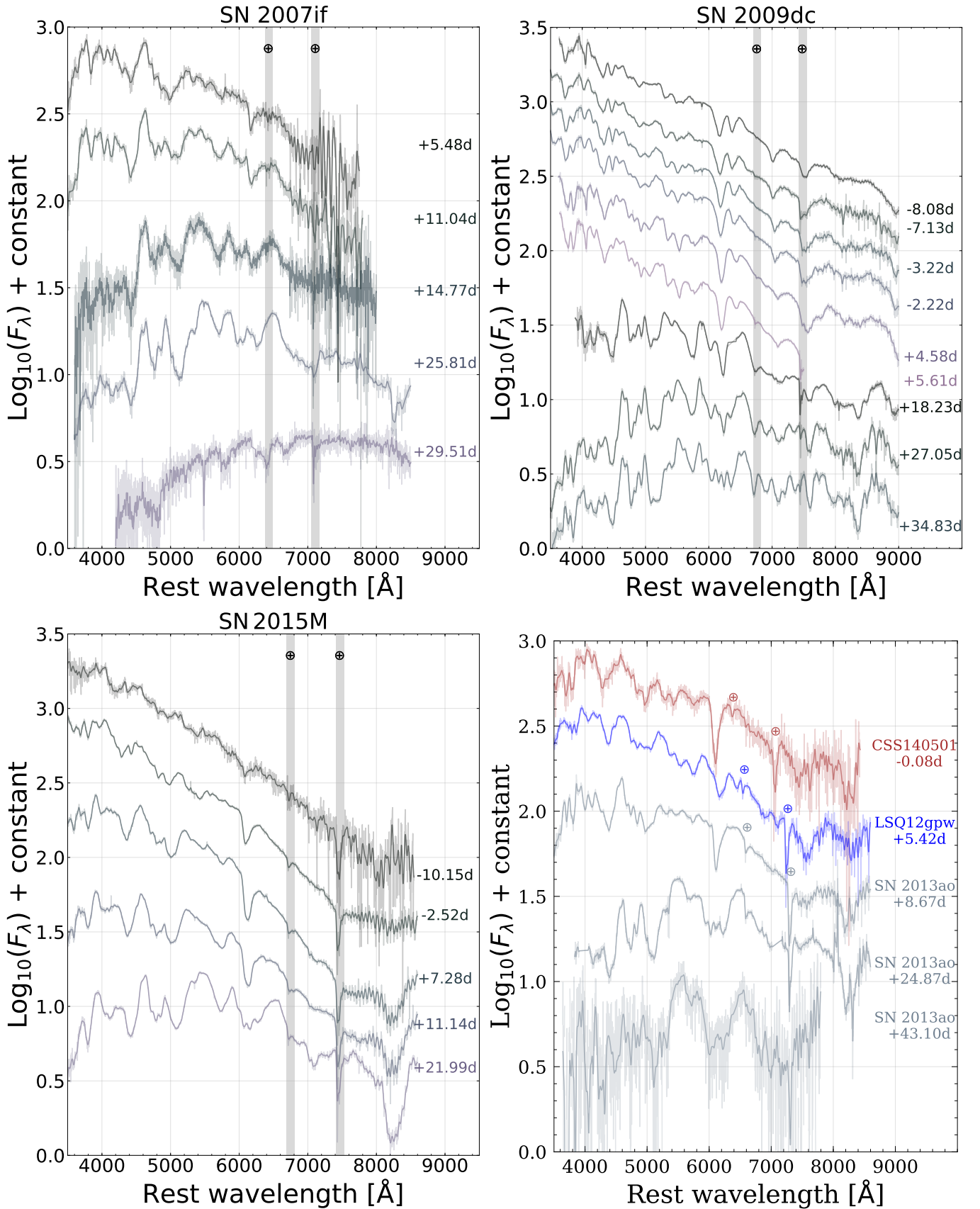


Figure 4. Rest frame optical spectra of all unpublished 2003fg-like SNe from the CSP. Rest frame phases relative to B -band maximum are given next to each spectrum. These data have not been corrected for extinction.

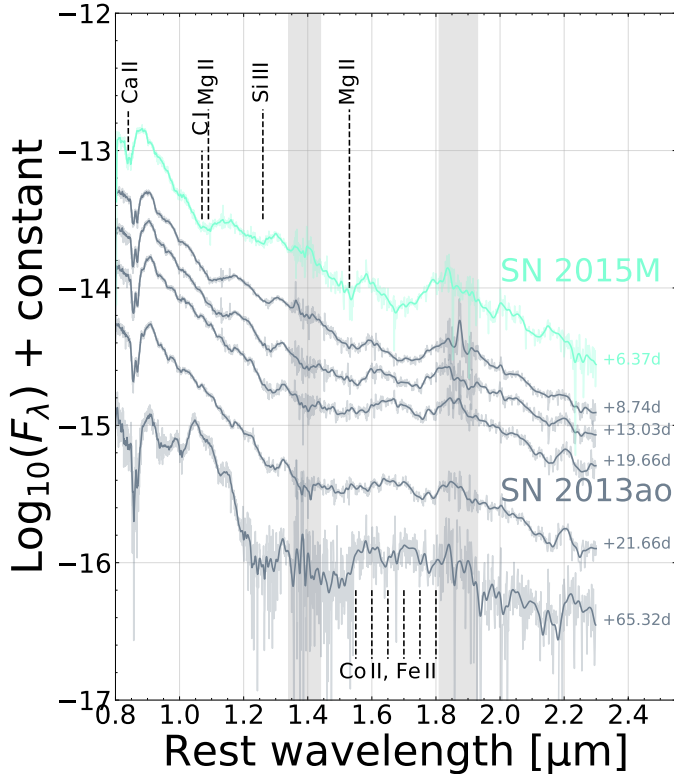


Figure 5. Rest frame NIR spectra of all unpublished 2003fg-like SNe from the CSP. Rest frame phases relative to B -band maximum are given next to each spectrum. Note that C I is only seen in the spectra of SN 2015M and not SN 2013ao. These data have not been corrected for extinction.

during the Lira tail, but be intrinsically different at early times and therefore have different luminosities demonstrating that for 2003fg-like SNe the Lira law is not reliable.

In Table 3, the values of extinction obtained with the two different methods are presented. As all of the methods mentioned above are highly uncertain, we choose to follow the conventional method of using the pEW of the Na I D feature. In the cases where the host $E(B - V)$ measurements based on the Na I D pEW are consistent with zero, no host extinction correction is employed. Furthermore, host galaxy extinction is only applied when explicitly stated in the following analyses.

5. PHOTOMETRIC PROPERTIES

5.1. Light curves

Figure 6 presents the K -corrected $BVri$ light curves of the sample compared to a selection of normal SN Ia ($\Delta m_{15}(B) < 1.3$ mag), all placed on the CSP natural system. The light curves are normalized to the peak, such that the comparison is in the light-curve shapes.

Table 3. EW values and limits of the Na ID feature, along with the $E(B - V)$ calculated from EW of the Na ID feature as well as from the ratio of the Balmer lines.

SN	Na ID EW	$E(B - V)^a$	$E(B - V)^b$
	Å	Mag	Mag
2003fg	0.33 ± 0.14	0.03 ± 0.03	...
2006gz	0.30 ± 0.11	0.03 ± 0.02	0.00
2012dn	0.27 ± 0.14	0.03 ± 0.02	...
ASASSN-15pz	≤ 0.05	0.00 ± 0.02	...
2007if	≤ 0.06	0.00 ± 0.02	...
2009dc	1.03 ± 0.24	0.23 ± 0.22	0.00
LSQ12gpw	0.23 ± 0.10	0.03 ± 0.02	0.23
2013ao	≤ 0.08	0.00 ± 0.02	0.09
CSS140126	≤ 0.42	0.00 ± 0.04	...
CSS140501	≤ 0.14	0.00 ± 0.02	0.00
LSQ14fmg	0.87 ± 0.44	0.15 ± 0.20	0.00
2015M	≤ 0.06	0.00 ± 0.02	...
ASASSN-15hy	≤ 0.06	0.00 ± 0.02	0.00

^aCalculated using relationship from Poznanski et al. (2012) with uncertainties as per Phillips et al. (2013).

^bCalculated from Balmer line ratio in IFS data from Galbany et al. (2021)

In the B and V bands, the 2003fg-like SNe are largely indistinguishable from normal SNe Ia, with some noted exceptions. SN 2007if, LSQ14fmg, and ASASSN-15hy have extremely slow rise times. Furthermore, LSQ14fmg declines rapidly at the start of the decay tail. Similarly rapid declines were also observed but at much later phases in SN 2009dc and SN 2012dn. CSS140126 also shows a hint of the rapid decline in the V band around the same phase as that of LSQ14fmg.

At redder wavelengths, the light curves of 2003fg-like SNe differ drastically from those of standard SNe Ia. In the r -band, 2003fg-like SNe have a much weaker post-maximum “knee”, except for LSQ14fmg. In the i -band, they have no strong secondary maxima, except in the case of CSS140126. The i -band secondary maximum has been suggested to be produced by the recombination of iron group elements in the ejecta (Höflich et al. 2002; Kasen 2006). Brighter SNe, such as 91T-like objects, tend to have a more prominent secondary i -band maximum, and fainter SNe, such as 91bg-like SNe, have a lack of a secondary i -band maximum. The latter case is caused by the merging of the primary and secondary maxima due to the quickly receding photosphere and a

small ^{56}Ni mass (see e.g., Höflich et al. 2002; Ashall et al. 2020).

For 2003fg-like SNe, the lack of a prominent i -band secondary maximum is a defining trait⁶. This suggests, unlike normal SNe Ia, that there is a lack of recombination of iron group elements in the ejecta at 2 d to 40 d past maximum. Given that 2003fg-like SNe are significantly brighter than sub-luminous SNe Ia, it is unlikely that the cause of the lack of a secondary i -band maximum is the same as in sub-luminous SNe Ia. In the case of 2003fg-like SNe, it suggests that a significant amount of luminosity is not produced by the radioactive decay ^{56}Ni , or that there is full mixing in the ejecta (e.g., Kasen 2006). However, as is seen in 2002cx-like SNe, if there were full mixing in the ejecta of 2003fg-like SNe we would expect to see a prominent H -band break and even lower ejecta velocities in the photoperic phase (e.g., Kromer et al. 2015; Stritzinger et al. 2015). Furthermore, if 2003fg-like SNe were powered predominately by the radioactive decay of ^{56}Ni it would be expected that they would have a very distinct secondary i -band maximum, such as in normal or 1991T-like SNe Ia. This is not the case for 2003fg-like SNe.

The NIR light curves of 2003fg-like SNe are vastly different than normal SN Ia (Fig. 7). Ten of the 2003fg-like SNe in the sample have NIR light curves. They are in general much brighter than the normal population in the NIR. None of the 2003fg-like SNe have a clear secondary maximum in the Y or H bands. The diversity between the 2003fg-like SNe is also large. For all 2003fg-like SNe, the phase of the NIR primary maxima occurs significantly after that of B -band maximum, whereas the NIR primary maxima of the normal population consistently transpires a few days before their B -band maxima. For example, the H -band light curve of SN 2012dn peaks ~ 50 d past B -band maximum. As a consequence, the NIR, specifically the H band, may be the most effective way to distinguish 2003fg-like SNe from normal SNe. These prolonged NIR light curves of 2003fg-like SNe imply that there could be some additional sources of luminosity (Nagao et al. 2017, 2018).

Another intriguing photometric peculiarity of 2003fg-like SNe is their UV luminosity. 2003fg-like SNe are ~ 2 mag brighter than normal SNe Ia in the mid-UV (Brown et al. 2014b). Brown et al. (2014b) analyzed the UV properties of SN 2009dc and SN 2012dn, which are located at opposite ends of the 2003fg-like SNe peak lu-

minosity distribution in the optical, and found that both of these objects peak at ~ -18 mag in the swift uvm2 band. Lu et al. (2021) analyzed the swift uvm2 light curves of all published 2003fg-like SNe and confirmed these results. The cause of this excess flux is unknown. It is not likely to be due to a larger amount of ^{56}Ni in the outer layers, as the ionization state of 2003fg-like SNe is generally low, and the H -band break is not observed until past +50 d from maximum light (Section 6.2). The high UV flux could be caused by low metallicity of the progenitor, where a low metallicity produces a lack of Fe-group elements in the outer layers and thus a lack of line blanketing (Mazzali et al. 2014). It could also be produced by an additional energy source which is not ^{56}Ni such as interaction with any surrounding material (e.g., Nagao et al. 2017; Hsiao et al. 2020). For a discussion on bolometric light curves see section 5.5.

Among the thirteen objects in the sample, six have early light curves (< -10 d) and constraints on the first epoch. The rise times of the two SNe from this work, CSS140501 and SN 2015M, are obtained by fitting the pre-maximum V -band photometry with a second order polynomial function, where the data was constrained by the discovery survey’s photometry and last non-detection limits as mentioned in Section A.1. The remaining the rise times were obtained from literature. The rise time of SN 2007if was obtained from an unfiltered magnitude (Scalzo et al. 2010). The rise time of SN 2009dc is given in the R -band (Silverman et al. 2011), and ASASSN-15hy (Lu et al. 2021) and ASASSN-15pz (Chen et al. 2019) are provided in the V -band. These SNe and their respective rise times are SN 2007if (24.2 ± 0.4 d; Scalzo et al. 2010), SN 2009dc (23 ± 2 d; Silverman et al. 2011), ASASSN-15pz (21.4 ± 2 d; Chen et al. 2019), ASASSN-15hy (22.5 ± 4.6 ; Lu et al. 2021), CSS140501 (20.9 ± 6.7 ; this work), and SN 2015M (19.8 ± 4.8 ; this work). This implies an average rise time of 22.0 ± 3.8 d.

5.2. Luminosity Width Relation

SNe Ia follow an intrinsic luminosity width relation (LWR), where brighter SNe have broader light curves. Two common ways to determine the broadness and the time scale of the light curve are the parameters $\Delta m_{15}(B)$ (Phillips 1993) or s_{BV} (Burns et al. 2014). $\Delta m_{15}(B)$ measures the change in B -band magnitude between maximum light and 15 rest-frame days past then, and s_{BV} is the time difference between the occurrence of B -band maximum and the reddest point in the $(B - V)$ color curve divided by 30 d (Burns et al. 2014).

To establish the location of 2003fg-like SNe on the LWR, the light-curve parameters were measured using

⁶ We note that CSS 140126 has a secondary i -band maximum but has a uncertain classification due to a low S/N spectra. However it fits into our sample because it peaks in the i -band after the B -band.

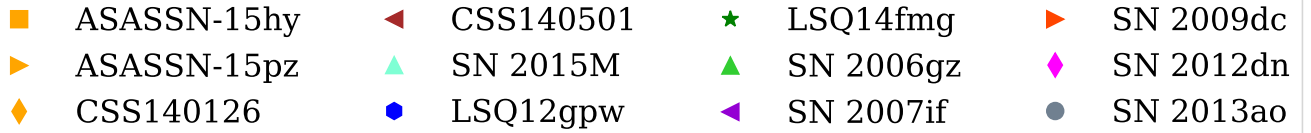
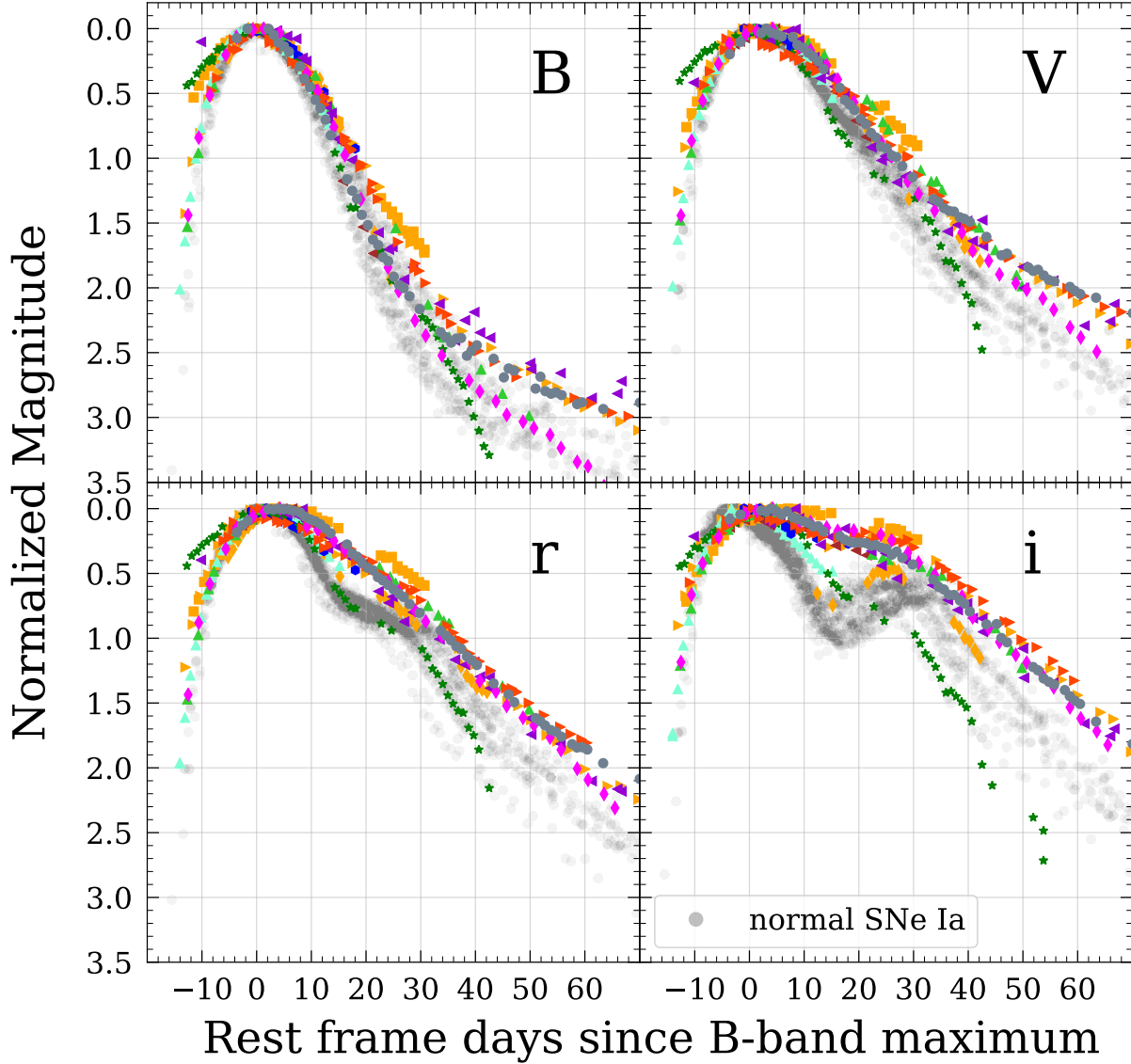


Figure 6. Comparison of $BVri$ -band light curves of the 2003fg-like SNe and normal SNe Ia. The light curves are presented relative to B -band maximum and in the rest frame. They have also been normalized to the peak of each respective band. Normal CSP SNe Ia are plotted in light grey for comparison. The selection criteria for the normal SNe are: $\Delta m_{15}(B) < 1.3$ mag and $E(B - V)_{host} < 0.15$ mag.

the *SNooPy* package (Burns et al. 2011). No light curve templates were used to fit the photometry or their derived parameters. Rather, the B_{max} , $\Delta m_{15}(B)$ and s_{BV} parameters were directly measured from the rest-frame K -corrected light curves interpolated with Gaussian processes. The *SNooPy* GET_COLOR function was used to calculate the color curves. For the color curves, no interpolation between data was performed when multi-band

observations on the same night were not available. The color curves were produced with Gaussian processes to obtain the time of the reddest point in the $(B - V)$ color curve relative to B -band maximum. This value was divided by 30 to obtain s_{BV} . This same technique was used to obtain the color curves in Section 5.3, and to derive the colors at maximum light. For all photometric measurements, uncertainties were obtained using

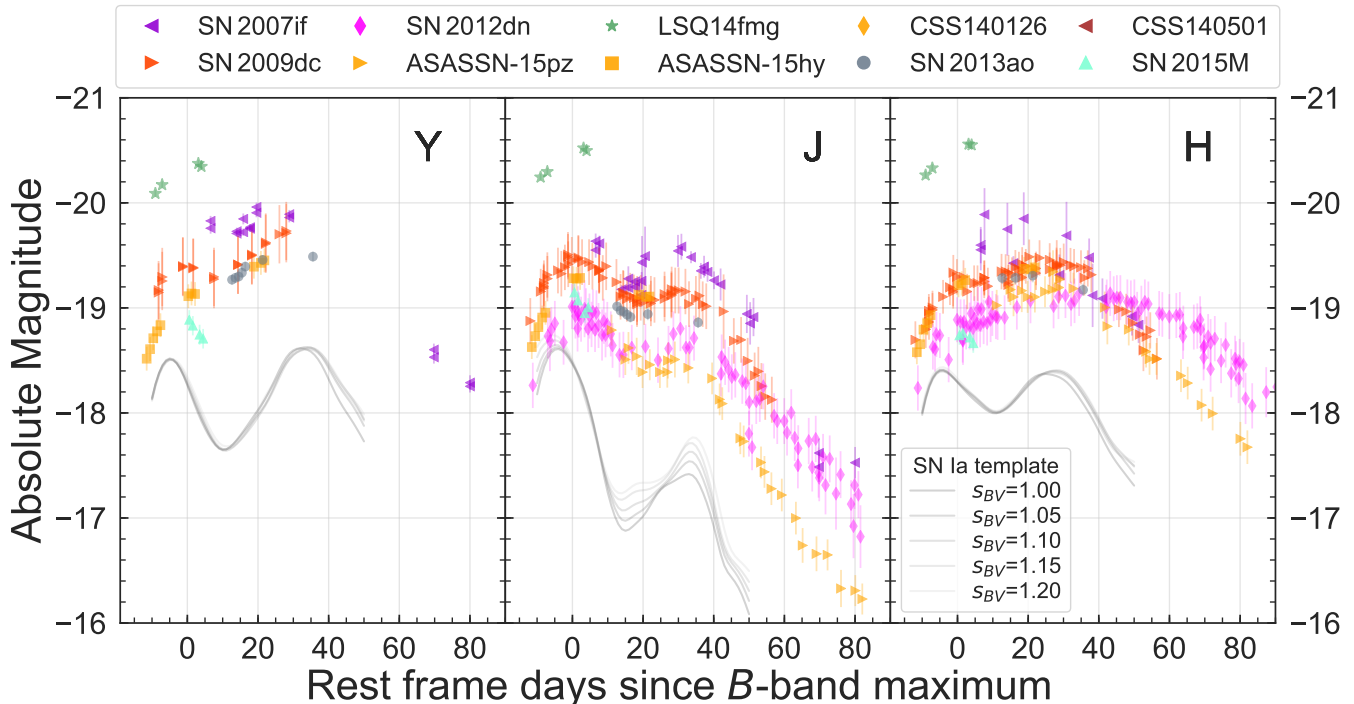


Figure 7. Absolute-magnitude YJH light curves of the 2003fg-like SNe in the sample. The light curves have not been K- or S-corrected. Normal SN Ia light-curve templates of $s_{BV}=1.00, 1.05, 1.10, 1.15,$ and 1.20 from *SNooPy* are plotted in grey colors for comparison, with the peak magnitude matching to the luminosity–decline rate relation from Fig. 4 of Burns et al. 2018. We chose not to normalize the NIR light curve comparison to peak as the time of the NIR maximum is uncertain for many objects. Overall, the NIR photometric properties of 2003fg-like SNe are distinct from those of normal SNe Ia.

a bootstrapping technique with 150 iterations. All rest frame, K-corrected, light curves were corrected for galactic and host extinction (where applicable). B_{max} was converted to M_B using the distance moduli presented in Table 1.

The B -band LWR as a function of $\Delta m_{15}(B)$ and s_{BV} is presented in the top panels of Fig. 8. The 2003fg-like SNe are all slowly declining with $\Delta m_{15}(B) < 1.3$ mag and $s_{BV} > 1$. 2003fg-like SNe are located below, above and in the same area of the LWR as normal SNe Ia. SN 2012dn, SN 2013ao, ASASSN-15pz, and SN 2015M are all located in the main part of the LWR. SN2006gz, LSQ12gpw and ASASSN-15hy are less luminous than their B -band light curve shape would imply if they were standard SNe Ia (i.e. they are less luminous than the LWR), whereas, SN 2007if, SN 2009dc, and LSQ14fmg are all brighter than the LWR. Unlike the previous suggestion of Taubenberger et al. (2011), it is evident with a larger sample that not all 2003fg-like SNe are overluminous. However, host galaxy extinctions of 2003fg-like SNe are highly uncertain and this may affect the location of some SNe on the LWR, although for the majority of points there is a reliable limit from the Na ID EW (Section 4). We note that most of our objects are within the

Hubble flow ($z > 0.02$) therefore the distance derived to the SN from the hosts are accurate.

The NIR is less affected by extinction, therefore it is a more suitable wavelength range to analyze any intrinsic luminosity differences between 2003fg-like SNe and other SNe Ia. We do not attempt to correct the NIR photometry for host extinction. The bottom panels of Fig. 8 show the LWR in the J and H bands. Unfortunately, the temporal coverage in the NIR is much worse than the optical. Therefore, for all SNe except SN 2009dc and SN 2012dn only lower flux limits can be set for the peak luminosity. The lower limits were determined by measuring the brightest photometric point on the rising light curves. In the J -band, most of the SNe are over luminous (brighter than -19 mag) except for ASASSN-15pz, CSS140126, and SN 2012dn that have a luminosity similar to that of normal SNe Ia. However for ASASSN-15pz and CSS140126 these values are lower limits on the luminosity and they could be intrinsically brighter. Interestingly, the H -band is the most effective wavelength range to distinguish between 2003fg-like SNe and normal SNe Ia. All of the 2003fg-like SNe are brighter than normal SNe Ia in the H band. They range from $M_H = -18.76$ mag (SN 2015M), to $M_H = -20.19$ mag (LSQ14fmg). The bright H -band is

one of the few ubiquitous properties of the subclass of 2003fg-like SNe. The fact that 2003fg-like SNe are not standardizable may suggest that there is more than one driving parameter driving the explosion. i.e. More than just a range of WD masses. There could be a range of both WD masses and envelope masses which produce 2003fg-like SNe see section 8 for a detailed discussion.

As shown by Galbany et al. (2021), 2003fg-like SNe are preferentially located in low metallicity and low mass galaxies with high sSFR, and are therefore more common in the high redshift universe. The fact that 2003fg-like SNe are not standardizable and they do not follow the LWR in the optical or NIR could have direct consequences for dark energy experiments. We have shown here that it is easier to remove 2003fg-like SNe from cosmological experiments with rest frame NIR data. But due to cosmic expansion, this strategy may limit future dark energy experiments to lower redshifts. With only near-maximum light, rest-frame, optical observations, 2003fg-like SNe may bias dark energy experiments. We briefly discuss this in Section 5.6. However, detailed simulations of this is outside the scope of this work.

5.3. Color curves

The observed color curves of the 2003fg-like SNe, corrected for Milky Way extinction, are shown in Fig. 9. At early times, the $(B - V)$ curves are similar to normal SNe Ia. They start red and reach their bluest point around maximum light. Between maximum light and +40 d, the ejecta cool until the reddest epoch is reached, after which the colors turn blue again. However, 2003fg-like SNe do not follow a tight Lira-like law (Phillips et al. 1999), and exhibit significant diversity. The reddest points in $B - V$ color curves cover a larger range (~ 0.7 - 1.3 mag) in 2003fg-like SNe than in normal SNe Ia. After the turnover, the 2003fg-like SNe events show a variety of gradients in the Lira tail. As discussed by Lu et al. (2021), ASASSN-15hy is unusual regarding its $(B - V)$ color curve. It does not get bluer during the early phase, and the evolution towards redder $(B - V)$ occurs much earlier than other SNe Ia. The ejecta begin to cool and get redder from ~ -10 d relative to B -band maximum, reaching $(B - V) \approx 0.2$ mag at maximum light. Lu et al. (2021) interpreted this to be caused by a lower ^{56}Ni mass explosion in the core degenerate scenario.

The $(r - i)$ color curves of 2003fg-like SNe show the largest diversity and generally do not behave like normal SNe Ia. There is a continuum of properties from LSQ14fmg which gets monotonically redder from the first measurement then stays flat after +25 d, to SN 2015M and CSS140126 which reach the bluest values. Generally, the 2003fg-like SNe start at similar $(r - i)$

values as normal SNe Ia, but do not reach such large negative values. More interestingly, at +50 d relative to maximum the 2003fg-like SNe $(r - i)$ color curves remain flat and in some cases continue to turn redder. This is caused by light curves at longer wavelengths in 2003fg-like SNe being much broader than normal SNe Ia. In large all-sky surveys such as ZTF and the Vera Rubin Observatory, analyzing the $(r - i)$ color curve up to +50 d may be one of the most effective ways to distinguish 2003fg-like SNe from the general population of SNe Ia.

5.4. s_{BV} vs. t_{max}^{i-B}

Ashall et al. (2020) demonstrated that the timing of the i -band primary maximum relative to the B -band maximum can be used as a powerful diagnostic to distinguish between sub-types of thermonuclear SNe. It was found that for 2003fg-like SNe the time of the primary i -band maximum was later than that of B band. Combining this information with s_{BV} was found to be an excellent way to identify 2003fg-like SNe. Fig. 10 shows the relation from Ashall et al. (2020) labeled with the 2003fg-like SNe from this work. Interestingly, ASASSN-15pz, which has a hint of an i -band secondary inflection, also has the smallest value of t_{max}^{i-B} . Although note that CSS140126 has both a strong i -band secondary maximum and a late t_{max}^{i-B} . Conversely, ASASSN-15hy has the largest value of t_{max}^{i-B} and no secondary i -band maximum. This may indicate a connection between the value of t_{max}^{i-B} and the presence of an i -band secondary maximum.

5.5. Bolometric light curves

Pseudo-bolometric light curves were constructed using observed photometry by employing the the direct method in *SNooPy*. Where needed, the observation gaps in between light curves were interpolated with Gaussian processes, but no extrapolations were applied outside the time range of individual light curves. Three wavelength regions were selected in order to explore the pseudo-bolometric peak luminosity and flux ratios in the UV, optical, and NIR. The light curve of a normal SN Ia 2007af (Krisciunas et al. 2017) was also constructed using the same method as above for comparison.

The $BVri$ (4200 to 7300 Å) pseudo-bolometric light curves are presented in the top panel of Fig. 11. The average peak luminosity in the sample is $L_{\text{peak}} = 10^{42.97 \pm 0.16}$ erg s $^{-1}$ for 11 2003fg-like SNe (SN 2003fg and LSQ12gpw are excluded due to their poor data coverage around the peak). When the NIR ($\sim \lambda 4200 - 16,000$ Å) is also included in the construction of the bolometric light curves 2003fg-like SNe peak at $L_{\text{peak}} =$

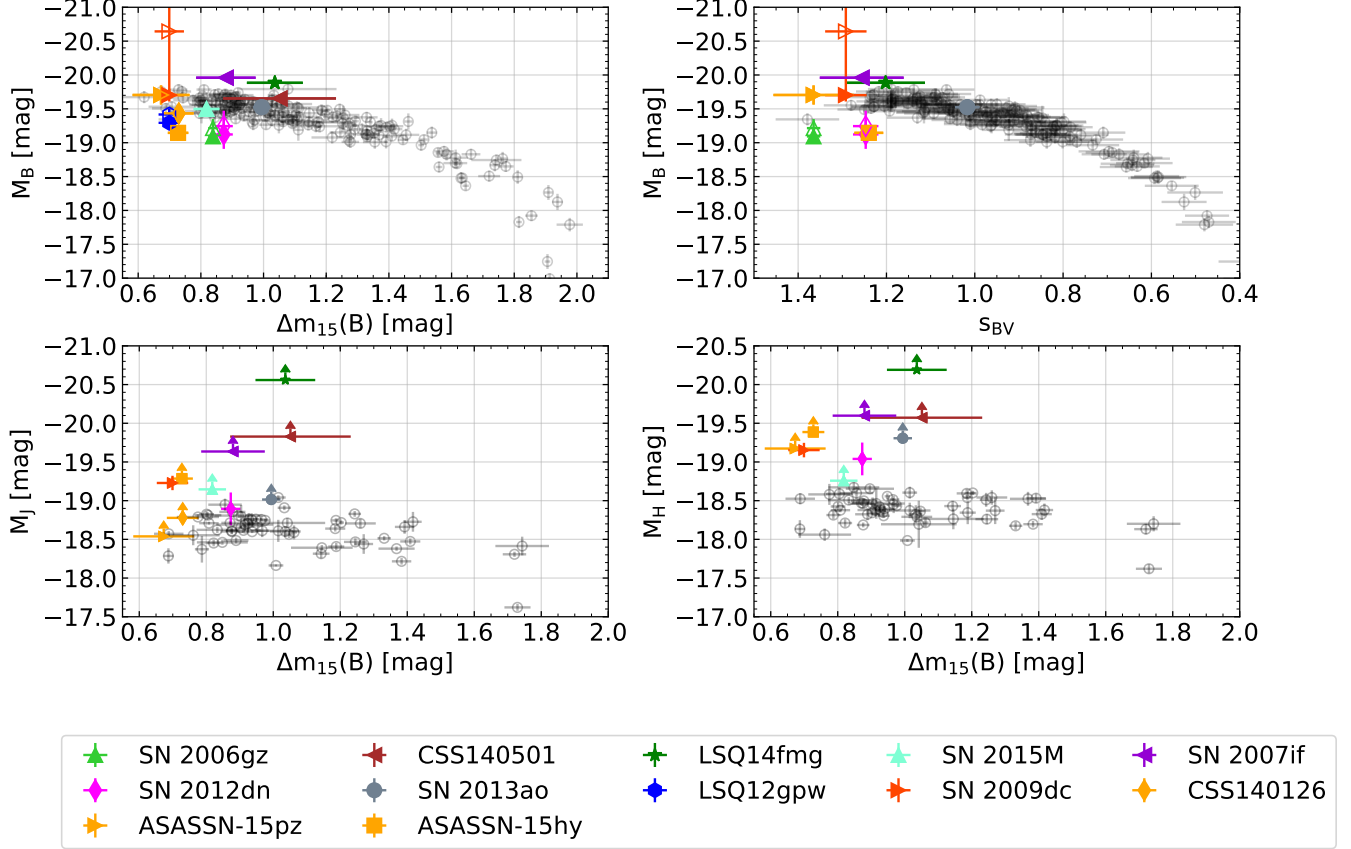


Figure 8. The luminosity width relation. *Top left:* The absolute B -band magnitude (M_B) plotted as a function of $\Delta m_{15}(B)$. *Top right:* M_B plotted as a function of s_{BV} . In both top panels the open symbols are corrected for galactic and host-galaxy extinction. *Bottom left:* M_J as a function of $\Delta m_{15}(B)$. *Bottom right:* M_H as a function of $\Delta m_{15}(B)$. For both of the bottom panels, many of the points are lower flux limits as the light curves are still rising during the final photometric observations. The 2003fg-like SNe points in the NIR LWR have not been corrected for host-galaxy extinction as the extinction in the NIR is negligible and the values of host-galaxy extinction are uncertain. In all plots the gray symbols are the LWR relation constructed using SNe Ia observed by the CSP (Krisciunas et al. 2017; Phillips et al. 2019).

$10^{43.16 \pm 0.22}$ erg s $^{-1}$ from the four SNe that have available peaks.

Interestingly, the fraction of flux in the NIR is generally higher in all 2003fg-like SNe compared to the normal SN Ia 2007af, as shown in the bottom panel in Fig. 11. This is consistent with 2003fg-like SNe having high NIR peak luminosities. All 2003fg-like SNe gradually increase in NIR flux fraction until one month after the maximum. It should be noted that SN 2012dn (which has the same luminosity as a normal SN Ia) shows the most prolonged and largest NIR contribution that persists well past +30 d.

For four 2003fg-like SNe it was possible to construct UV and NIR ($\sim \lambda 2200 - 16,000$ Å) pseudo-bolometric light curves. Both ASASSN-15hy and SN 2012dn have a peak luminosity of $L_{\text{peak}} = 10^{43.17 \pm 0.01}$ erg s $^{-1}$. Despite the small size of the sample, the effect of the bright UV and NIR as well as the flux redistribution are clearly demonstrated (see Fig. 12). In 2003fg-like SNe there is

no increase in UV flux at early times, unlike in normal SN Ia. The UV fraction of the bolometric flux is already declining when 2003fg-like SNe were first observed, while the UV fraction increases until just before maximum light for normal SNe Ia. The 2003fg-like SNe also show a low optical ($\sim \lambda 4200 - 7300$) luminosity fraction and high NIR ($\sim \lambda 7300 - 16,000$) fraction compared to the normal SN Ia 2007af.

5.6. Hubble residuals

While the exact rate of 2003fg-like SNe is unknown they are extremely rare and make up a very small fraction of SNe Ia in the local universe. However, they prefer low-mass and high specific star forming host galaxies both of which will increase their fraction in high-redshift SNe surveys. They do not follow the LWR, have broad light curves, and some 2003fg-like SNe are not overluminous and overlap normal SNe Ia in peak brightness. Furthermore, in the rest frame B and V bands, it is dif-

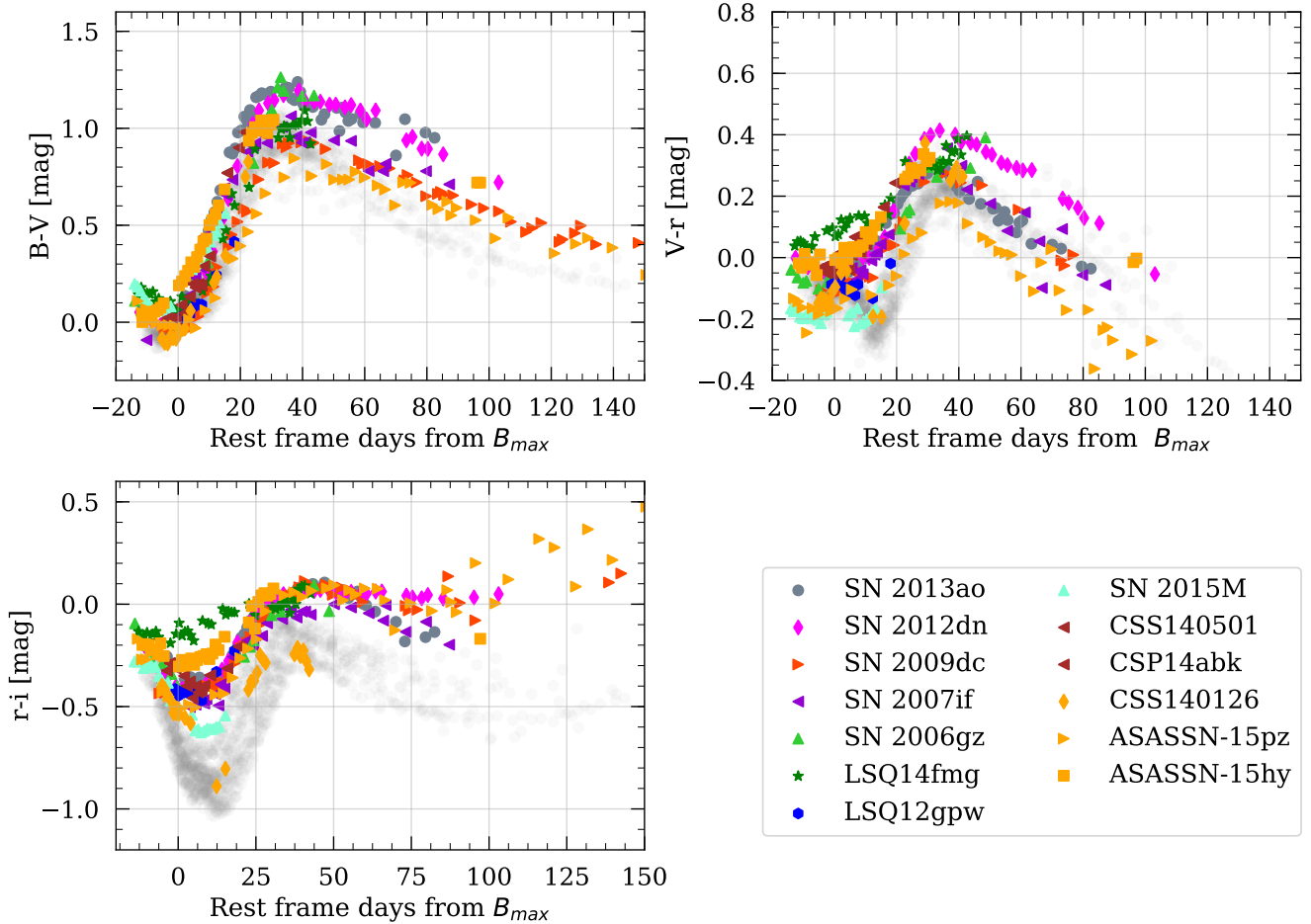


Figure 9. The observed color curves of our 2003fg-like SNe sample corrected for Milky Way extinction (solid markers) and compared to a sample of normal SNe Ia from the CSP (light gray). The normal SNe Ia were selected so they have $\Delta m_{15}(B) < 1.3$ mag and an $E(B - V)_{host} < 0.15$ mag. The $B - V$ color curves of 2003fg-like SNe are similar to those of normal SNe Ia, yet the $r - i$ color curves differ significantly. All curves have been corrected for Galactic extinction, but not host galaxy extinction.

difficult, if not impossible, to distinguish 2003fg-like SNe from normal SNe Ia. Therefore, 2003fg-like SNe have the potential to bias dark energy experiments. Although a full simulation of this is beyond the scope of this paper, we determine what the Hubble residuals would be if 2003fg-like SNe were treated as normal SNe Ia and fit with light-curve fitting tools.

To determine the Hubble residual for each 2003fg-like SNe, we used the *SNooPy* *EBV_model2*, with *st* (which is the input setting for s_{BV}) as the light curve shape parameter. To ‘simulate’ the effect of future dark energy experiments such as those from the Nancy Grace Roman Space Telescope, we fit the light curves from +0 to +30 d relative to B -band maximum. The light-curve fitting is done twice, once with only the B - and V -bands and then with all of the bands from UV to NIR. For both fits, most of the 2003fg-like SNe have negative Hubble residuals (see Table 4). This implies that when

run through light curve fitters, 2003fg-like SNe are too bright for their light curve shape. Fig. 13 presents the Hubble residuals as a function of light-curve decline rate. The mean residuals are $\Delta\mu(all) = -0.74 \pm 0.02$ mag and $\Delta\mu(BV) = -0.48 \pm 0.50$ mag. The Hubble residuals are generally smaller and the light curves fit better to the templates when only the B and V bands are used. Thus, in the case that only rest-frame B and V bands are observed, 2003fg-like SNe may not be identified and removed in dark energy experiments and will cause a bias. A more detailed simulation is warranted to determine the true extent of this contamination and is beyond the scope of this work.

6. SPECTROSCOPIC PROPERTIES

In this section, the spectroscopic properties of 2003fg-like SNe are presented. First, we concentrate on optical

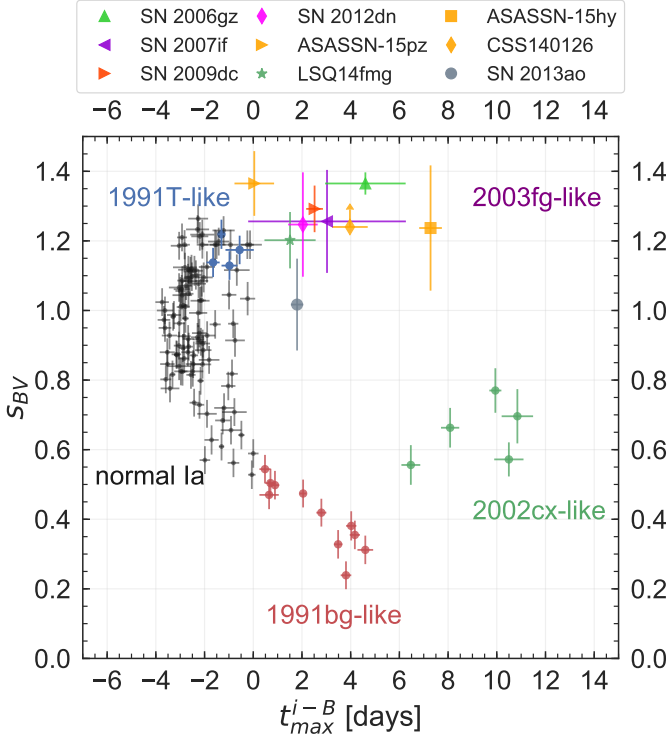


Figure 10. The time of the i -band maximum relative to the B -band maximum vs. s_{BV} with data taken from Ashall et al. (2020) and 2003fg-like SNe of this work. These values do not include K-corrections since they are of various subtypes, this is also consistent with the analysis of Ashall et al. (2020). All of the 2003fg-like SNe are located in the top right corner of the figure.

wavelength spectra and line identifications. Then we discuss the NIR spectra and their line identifications. The velocity and pseudo equivalent width (pEW) measurements, and properties including the Branch diagram are then presented.

6.1. Optical wavelength spectra

All available maximum light and +20 d spectra of 2003fg-like SNe are presented in Fig. 14. At maximum light, the spectra show the standard lines associated with SNe Ia (e.g., Branch et al. 2006; Ashall et al. 2018), see table 5. Many of the 2003fg-like SNe also have strong C II $\lambda 6580$ and $\lambda 7234$ features persisting through maximum light. 2003fg-like SNe also have weak Ca II features at this phase. By +20 d from maximum light the Ca II feature is much stronger, and the spectrum contains no residual C II.

The maximum light and +20 d spectrum of SN 2009dc and SN 2013ao are compared to a variety of sub-types of SNe Ia in Fig. 15. SN 2009dc and SN 2013ao were chosen for this comparison as they are located at the extreme ends of the luminosity parameter space. Both

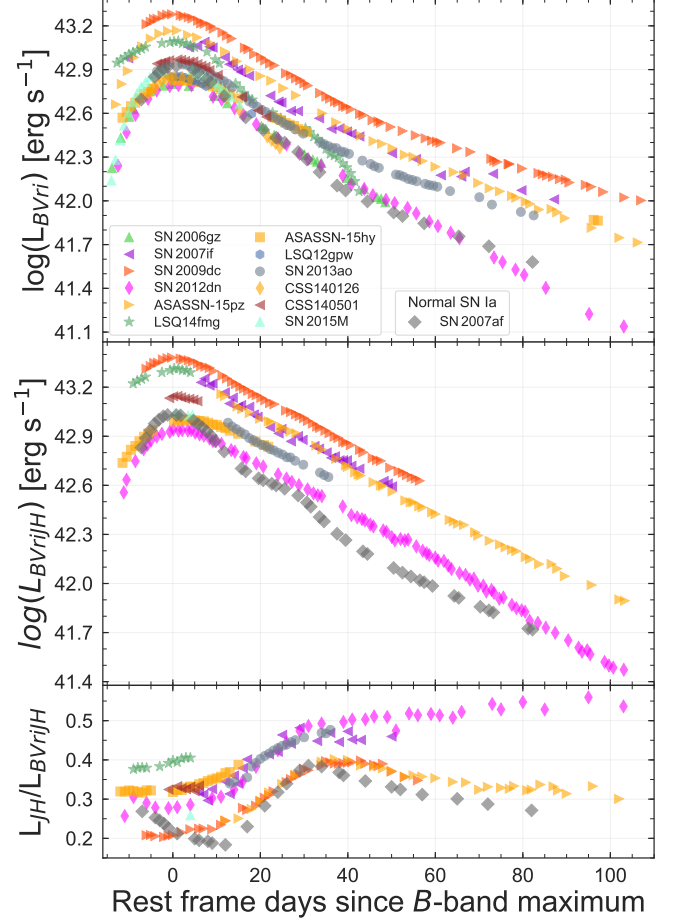


Figure 11. Pseudo-bolometric light curves of 2003fg-like SNe. The top panel shows the Pseudo-bolometric light curves constructed with optical $BVri$ bands, the middle panel presents those with optical $BVri$ and NIR JH bands, and the bottom panel displays the fraction of the NIR luminosity.

SN 2009dc and SN 2013ao appear to have slightly weaker or “washed out” spectral features compared to the other SNe. However, in terms of ionization state SN 2013ao appears to be most similar to SN 2006bt (Foley et al. 2010), and SN 2011fe (Mazzali et al. 2014). With maximum light spectra alone, it is almost impossible to distinguish between SN 2013ao and the normal SN 2011fe, and the only noticeable difference are weaker Ca II features in SN 2013ao. On the other hand, SN 2009dc has a similar ionization state to SN 2013ao, but also has strong C II absorption and lower velocities, as is seen with the Si II $\lambda 6355$ feature. Although SN 2009dc appears to be as blue as SN 1991T, the lack of Fe III and a stronger Si II $\lambda 5972$ feature demonstrate that the ionization state in the line forming region of SN 2009dc is lower.

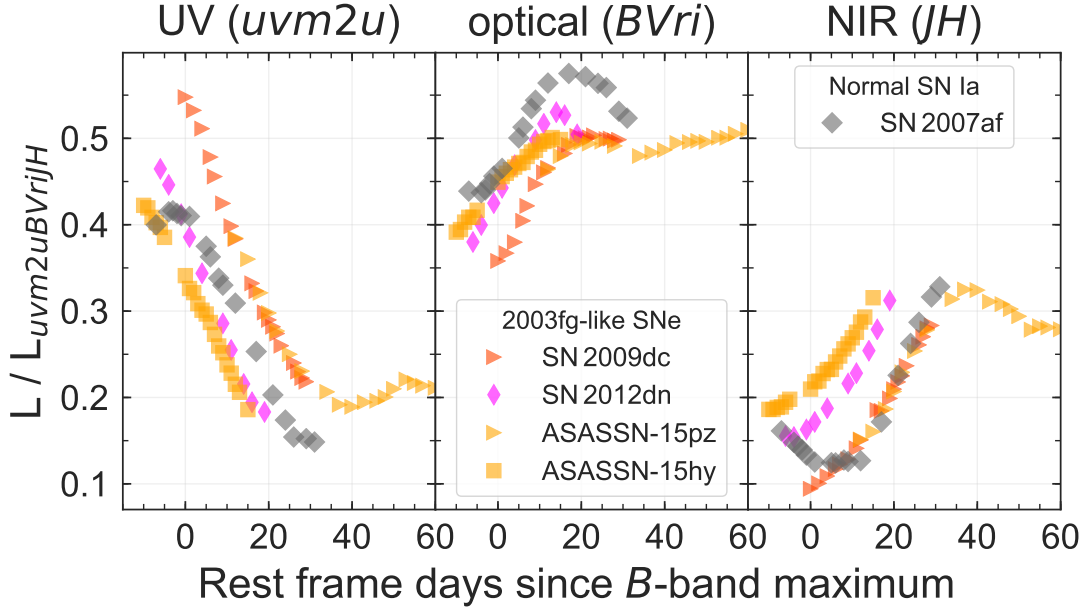


Figure 12. Fractions of pseudo-bolometric luminosity of 2003fg-like SNe in UV ($\sim \lambda 2200 - 4200$), optical ($\sim \lambda 4200 - 7300$) and NIR ($\sim \lambda 7300 - 16,000$) regions. Unlike normal SNe Ia that have the optical region accounting for $\sim 80\%$ of the luminosity, 2003fg-like SNe all show a significant fraction of luminosity in the UV and NIR. The time evolution of the fractions also shows the flux redistribution from UV to NIR.

Table 4. The Hubble residual of the 2003fg-like SNe in the sample. The values were calculated using *SNooPy EBV_model2* and compared to the CMB corrected redshift distance. The cosmological parameters used for this section are $H_0 = 73 \text{ km s}^{-1} \text{ Mpc}$, $\Omega_m = 0.27$, $\Omega_\Lambda = 0.73$. The Hubble residuals were computed using two cases: 1) B and V bands only and 2) all of the available bands ($uvuBVgrizYHJ$).

SN	$\Delta\mu(BV)$ Mag	$\Delta\mu(all)$ Mag
2003fg
2006gz	0.21 ± 0.09	0.18 ± 0.04
2012dn	0.08 ± 0.05	-0.32 ± 0.02
ASASSN-15pz	-0.24 ± 0.09	-0.84 ± 0.03
2007if	-1.35 ± 0.09	-1.66 ± 0.04
2009dc	-0.13 ± 0.04	-0.99 ± 0.02
LSQ12gpw	-0.15 ± 0.09	-0.15 ± 0.08
2013ao	-0.99 ± 0.03	-0.51 ± 0.03
CSS140126	0.00 ± 0.11	-0.37 ± 0.03
CSS140501	-1.20 ± 0.07	-1.15 ± 0.04
LSQ14fmg	-0.72 ± 0.06	-1.77 ± 0.08
2015M	-0.78 ± 0.03	-0.55 ± 0.02
ASASSN-15hy	-0.44 ± 0.05	-0.71 ± 0.03

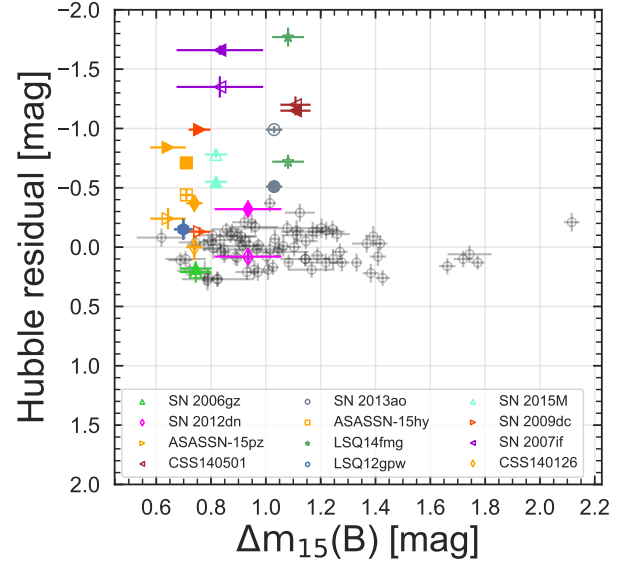


Figure 13. Hubble residuals of a selection of normal SNe Ia from the CSP (black open markers) and of the 2003fg-like SNe fit with both the B and V bands (open symbols) and all available bands (solid symbols). The Hubble residuals are smaller if only the B and V bands are used.

Hachinger et al. (2012) claim these “washed out” features and the low ionization state in 2003fg-like SNe are produced by an additional thermal luminosity source, which is H/He deficient. Hsiao et al. (2020) suggest that this could be due to interaction with a C-O envelope in the core degenerate scenario. Taubenberger et al. (2019)

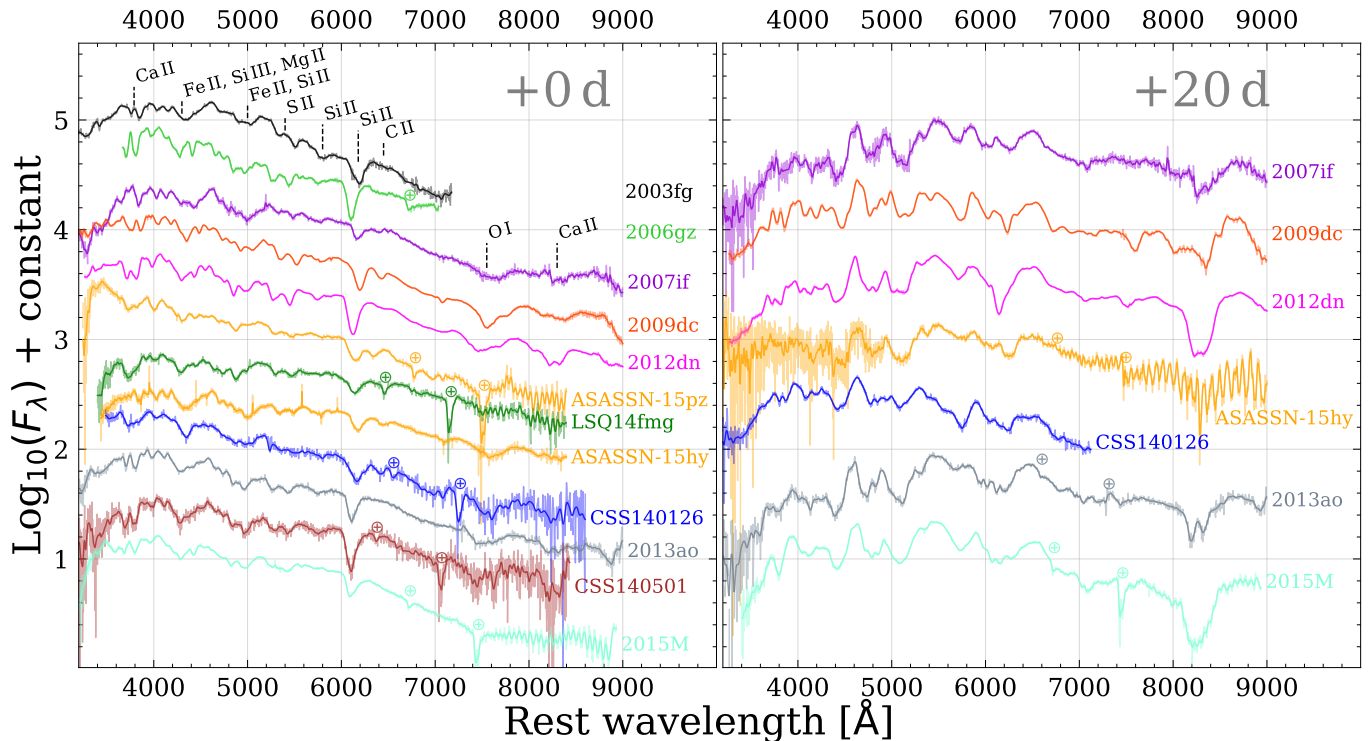


Figure 14. *Left panel:* Maximum light spectra of all of the 2003fg-like SNe in the sample. *Right panel:* 2003fg-like SNe spectra at +20 d for objects which have spectra at this phase.

Table 5. The main spectra lines identified in the 2003fg-like SNe spectra at maximum light.

Ion	Wavelength
	Å
Ca II	$\lambda\lambda 3968, 3933$
Si II	$\lambda 4130$
Mg II	$\lambda 4481$
Si III	$\lambda 4552$
Fe II	$\lambda 5169$
Fe III	$\lambda 5156$
S II	$\lambda 5453, \lambda 5606$
Si II	$\lambda 5972, \lambda 6355$
O I	$\lambda 7771$
Ca II	$\lambda\lambda 8498, 8542, 8662$

propose that it could be caused by the violent merger of two WDs, although the low continuum polarization makes the latter unlikely (Tanaka et al. 2010; Cikota et al. 2019).

At +20 d, the spectra of all sub-types of SNe Ia are similar. All of the 2003fg-like SNe and comparison SNe Ia except SN 2013ao have an emission feature in the 5900 Å region. This feature has been attributed to either [Co III] 5888 Å (Dessart et al. 2014) or Na I D emission (Mazzali et al. 2008). If this feature is attributed to [Co III], the lack of this emission in SN 2013ao may be caused by the lack of ^{56}Ni above the photosphere. This is consistent with the lack of an *H*-band break in the NIR spectra of SN 2013ao. Note however that SN 2009dc, SN 2015M, and ASASN-15hy do not have an *H*-band break at these epochs, but all show this emission feature at 5900 Å. We thus conclude that the feature is more likely caused by Na I D emission, which is not seen in SN 2013ao due to higher temperature and density in the ejecta. Alternatively, differences in the progenitor configuration, including metallicity differences, could produce a reduced Na abundance.

One of the easiest ways to distinguish between 2003fg-like SNe and other sub-types of SNe Ia is with spectra at -10 d with respect to maximum light (Fig. 16). At this epoch, 2003fg-like SNe have weak features and are dominated by continuum, Si II absorption, and have very weak or no Ca II and Fe III features. On the other hand, SN 2011fe is redder and has strong P Cygni profiles which include a large amount of intermediate mass elements such as a strong Si II $\lambda 6355$ and Ca II features.

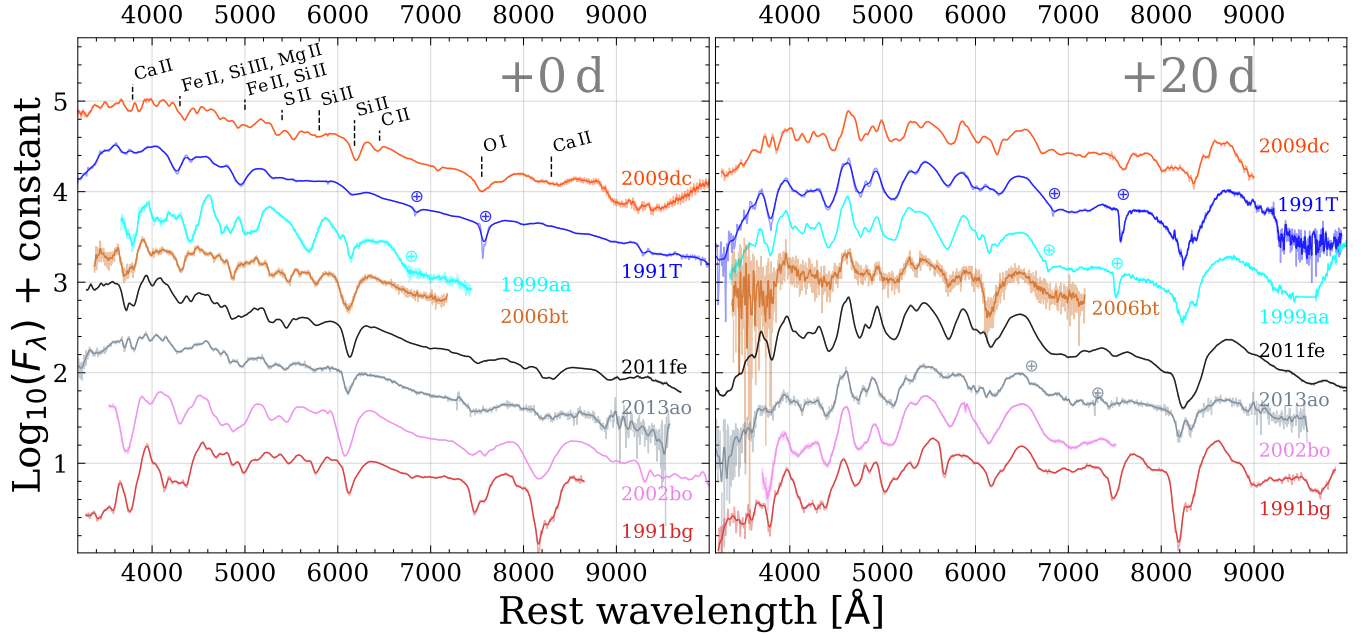


Figure 15. Comparison between maximum light (*left*) and +20 d (*right*) spectra of the over-luminous 2003fg-like SN 2009dc and an under-luminous one (SN 2013ao) along with a selection of other SNe Ia sub-types.

Similar to 2003fg-like SNe, SN 1991T has a hot continuum and no Ca II features. However, SN 1991T has a strong Fe III feature at ~ 4900 Å and no C II absorption, which is unlike 2003fg-like SNe. With this in mind, we suggest that the lack of a strong Fe III absorption in early-time spectra should become one of the defining characteristics of 2003fg-like SNe.

Several hundred days post explosion, the ejecta of SNe are optically thin and dominated by forbidden transitions (see Taubenberger et al. 2019). The ionization state of these lines provides critical information about the rate of recombination and the density in the center of the explosion. Normal SNe Ia have nebular spectra which are dominated by strong [Fe III] at ~ 4700 Å and a weaker [Fe II] emission at ~ 5200 Å, with an [Fe II]/[Ni II]/[Ca II] emission at ~ 7300 Å (e.g., Graham et al. 2017). Luminous SNe Ia, such as SN 1991T, have a higher ionization state with strong [Fe III] lines (Cappellaro et al. 2001), and sub-luminous SNe Ia tend to have a stronger [Ca II] and weaker [Fe III] emission than normal SNe Ia (e.g., Mazzali & Hachinger 2012; Galbany et al. 2019).

Four 2003fg-like SNe, SN 2006gz (Maeda et al. 2009), SN 2007if (Taubenberger et al. 2013b), SN 2009dc (Taubenberger et al. 2013b), and SN 2012dn (Taubenberger et al. 2019) have nebular phase spectra. Interestingly, despite being luminous, all of these objects show a low ionization state with weak [Fe III] emission. They also have strong [Ca II] emission. SN 2012dn (the least luminous of the four) has the strongest [Ca II] emission,

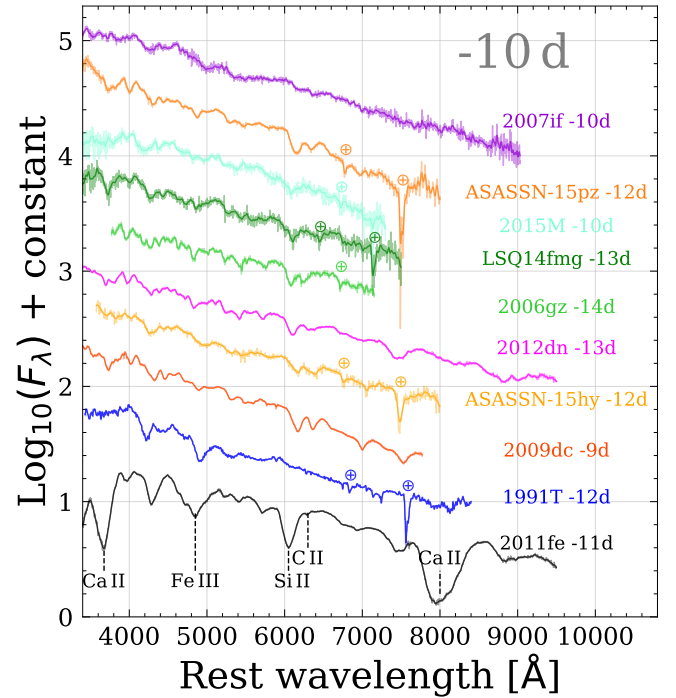


Figure 16. Early-time spectroscopic comparison between 2003fg-like SNe, the normal SN 2011fe, and the over-luminous SN 1991T. All 2003fg-like SNe with adequate data tend to show strong C II and no significant Fe III. In contrast, SN 1991T has strong Fe III and SN 2011fe generally has stronger features. In these phases, it is possible to distinguish 2003fg-like SNe from other sub-types of SNe Ia.

significantly stronger than the other 2003fg-like SNe. SN 2012dn also shows [O I] emission at 6300 Å, which has only been observed in the nebular phase spectra of one other SN Ia, the sub-luminous SN 2010lp (Taubenberger et al. 2013a). Although sub-luminous and 2003fg-like SNe sit at the opposite ends of the LWR they share similar traits in nebular phase spectra of low-ionization state and strong [Ca II] emission. However, in 2003fg-like SNe the low ionization is likely caused by low ejecta velocities (see section 6.3), high central densities, and an increased recombination rate; whereas in the sub-luminous SNe Ia (e.g., SN 1986G; Phillips et al. 1987; Ashall et al. 2016), the low ionization state is thought to be caused by less heating owing to their smaller ^{56}Ni masses.

6.2. NIR spectra

NIR spectroscopy provides critical information on the physics of SNe Ia (e.g., Kirshner et al. 1973; Marion et al. 2009; Hsiao et al. 2019). In the NIR, the photosphere recedes faster than at shorter wavelengths, allowing for deeper parts of the ejecta to be exposed at earlier times. The NIR also contains different ions than the optical, such as C I 1.0693 μm and the H -band break ($\sim 1.4\text{--}1.9\ \mu\text{m}$). If 2003fg-like SNe contain a large carbon shell, it would be expected that as the ejecta cool, the ionization state of carbon would transition from singly ionized to neutral. Given that the carbon shell is large and generally dominated by C II which is seen up to and past maximum light it is expected that there would be strong NIR C I well past maximum light. This is seen in SN 2015M that shows a distinct C I 1.0693 μm absorption at $\sim 11\ 000\ \text{km s}^{-1}$ (see Fig. 5). C I may also be seen in ASASSN-15hy (see Lu et al. 2021). For the 2003fg-like SNe objects which do not show C I, either the carbon has become optically thin, stays ionized at all epochs, or the C I line is very weak possibly due to the presence of He in the outer layers as discussed in the Appendix D of Lu et al. (2021).

The H -band break is formed from a multiplet of allowed Co II, Fe II, and Ni II emission lines located well above the photosphere (Wheeler et al. 1998; Höflich et al. 2002). The strongest and bluest of these lines is Co II 1.57 μm . The H -band break appears when the photosphere recedes into the ^{56}Ni region. For normal SNe Ia, this begins a few days after maximum light, and for sub-luminous SNe Ia, the break emerges slightly later, at $\sim +8$ d. The later appearance can be interpreted as the photosphere having to recede through more material to reach the ^{56}Ni region. The strength of the H -band break correlates with light curve shape, where brighter SNe have a stronger break (Hsiao et al. 2013). Fur-

thermore, the velocity of the bluest edge (v_{edge}) of the H -band region at 10 ± 3 d can be used to directly measure the edge of the ^{56}Ni region in a SN Ia (Ashall et al. 2019a), where more luminous SNe Ia have larger values of v_{edge} . v_{edge} can be used to discriminate between SNe Ia explosion models (Ashall et al. 2019b).

Fig. 17 shows the NIR spectra of the four 2003fg-like SNe which have spectra at 10 ± 3 d, as well as the 1991T-like LSQ12gdj and the normal SN 2011fe. Unlike normal, sub-luminous, and 1991T-like SNe Ia, 2003fg-like SNe show a very weak or no H -band break by +10 d. The lack of an H -band break indicates that the photospheres of 2003fg-like SNe have not receded into the ^{56}Ni region by this time and that the mass above the ^{56}Ni is large. As 1991T-like SNe Ia have a higher ionization state but still have a strong H -band break, an ionization effect can be ruled out as the cause of their lack of H -band break. We note that although sub-luminous SN Ia have a weak H -band break it is intrinsically different from the H -band break in 2003fg-like SNe. SN 2009dc and ASASSN-15hy have NIR spectral observations that extend to +85 and +80 d past maximum, respectively. In these SNe the break appears at much later epochs. In SN 2009dc, the H -band break appears between +24 and +85 d (Taubenberger et al. 2011), and in ASASSN-15hy, it appears between +30 d and +80 d (Lu et al. 2021). The delayed onset of the H -band break demonstrates that the ^{56}Ni region is in the very inner layers of the ejecta and the photosphere has to recede through a large optically thick envelope before reaching the bulk of the ^{56}Ni . With this in mind in the next section we will measure the velocities and pEWs of the early time spectra to determine the chemical composition and structure of 2003fg-like SNe.

6.3. Velocity and pEW fitting method

For the optical wavelength spectra, the velocity minima and pEW of the main spectral features were obtained using the Measure Intricate Spectral Features In Transient Spectra (misfits⁷; S. Holmbo et al., in prep.) code. To acquire the minimum of a P Cygni absorption feature, the rest frame spectra were smoothed by passing them through a low-pass filter after Fourier transforming them to remove the high-frequency noise, as described in Marion et al. (2009). An error spectrum was computed by obtaining the differences between the observed spectra and the Fourier transformed smoothed spectrum. The absolute values of the residuals are smoothed with a Gaussian function. The corresponding Gaussian

⁷ <http://github.com/sholmbo/misfits>

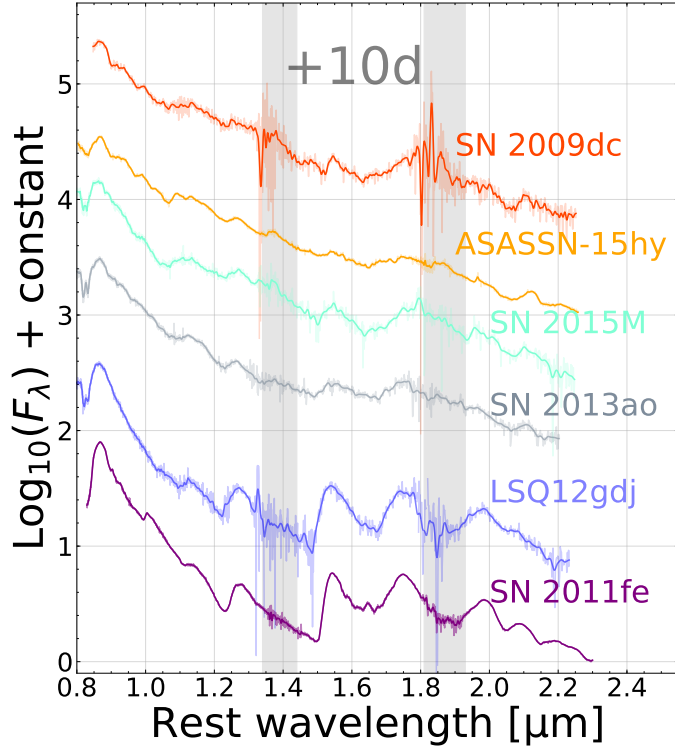


Figure 17. The NIR spectra of four 2003fg-like SNe, as well as the 1991T-like LSQ12gdj and the normal SN 2011fe around +10 d past maximum light. None of the four 2003fg-like SNe show a strong H -band break. For presentation purposes the spectra have been interpolated with a gaussian filter having a 3-sigma smoothing length.

smoothed version that is scaled contains 68% of the absolute value of the residual level and is used as the 1-sigma error spectrum.

The *velocity.gaussians* function was utilized to obtain the minimum of an absorption feature. The boundaries of the wavelength region were manually selected for each feature. A linear continuum and a single Gaussian function were simultaneously fit to the feature, and the best fit was determined by chi-squared minimization. To estimate the uncertainty, a Monte Carlo approach was adopted with 1000 realizations. The realizations were generated by including the flux uncertainty assuming a normal distribution and the boundary uncertainties assuming a uniform distribution. The minimum wavelengths were converted to velocity using the relativistic Doppler formula and rest wavelength of the feature. The mean and the standard deviation of the velocities measured from the Monte Carlo realization were adopted as the value and the 1σ uncertainty of the velocity, respectively.

The pEW of the features was calculated following the prescription of Garavini et al. (2007). The

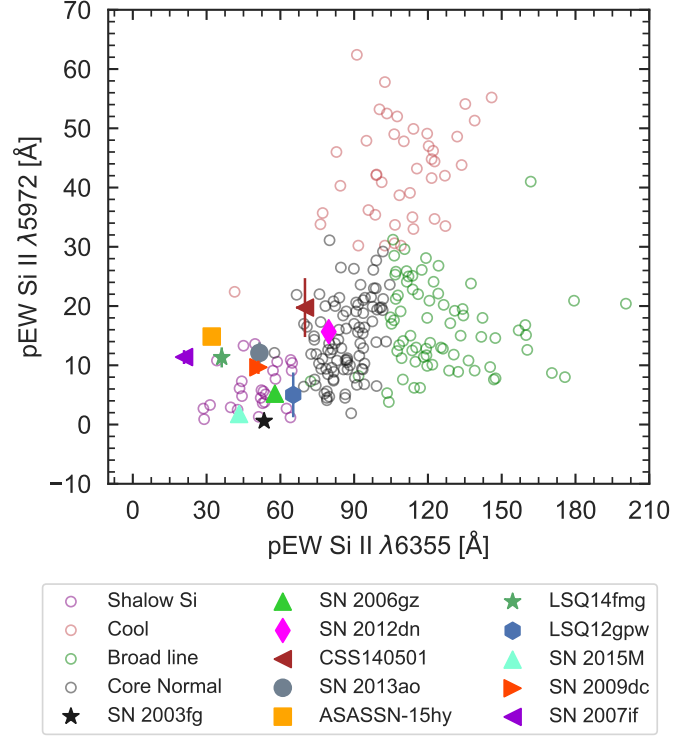


Figure 18. The Branch diagram produced using SN Ia data from Blondin et al. (2012) and Folatelli et al. (2013). Most 2003fg-like SNe are located within the same area as the shallow silicon (SS) SNe Ia.

width.shallowpew function was used in *misfits*, where uncertainties were determined with the same Monte Carlo method mentioned above. The mean value and standard deviation were taken as the pEW and its 1σ uncertainty.

6.4. Velocity and pEW measurements

In this work, the pEW of Si II $\lambda 5972$, $\lambda 6355$ and C II $\lambda 6580$ were measured, as well as the velocity of Si II $\lambda 6355$ and C II $\lambda 6580$. The pEW of the $\lambda 6355$ and $\lambda 5972$ Si II features have been shown to be a powerful diagnostic to identify SN Ia sub-types, where normal SNe Ia can be separated into four groups, (core normal, shallow Si, broad line and cool Branch et al. 2006; Burrow et al. 2020). In this parameter space, most 2003fg-like SNe are located primarily in the shallow-silicon area close to over luminous objects such as 1991T-like objects (see Fig. 18). However, SN 2012dn and CSS140501 are in a similar area as core normal SNe. These two SNe also overlap with the normal population in the LWR (Fig. 8).

The bottom panels of Fig. 19 show the velocity of the C II $\lambda 6580$ and Si II $\lambda 6355$ features as a function of time. The velocities decrease over time as would be expected from a homologous expansion and a receding photo-

sphere. The velocity spread in Si II $\lambda 6355$ between the fastest and slowest 2003fg-like SNe is $5,000 \text{ km s}^{-1}$. At the earliest epochs, around -10 d , the velocities range from $\sim 13,500 \text{ km s}^{-1}$ (SN 2006gz) to $\sim 8,000 \text{ km s}^{-1}$ (SN 2007if), and by maximum light the spread has decreased to $11,500 \text{ km s}^{-1}$ for the fastest expansion and $7,500 \text{ km s}^{-1}$ for the slowest. Despite the large spread, some 2003fg-like SNe exhibit some of the slowest velocities of any SN Ia. The change in velocity from the -10 d to maximum light roughly indicates the depth of the Si shell. The change in Si II $\lambda 6355$ velocity between -10 d to maximum light ranges from $2,000 \text{ km s}^{-1}$ in SN 2006gz, to $1,000 \text{ km s}^{-1}$ in SN 2012dn, and 0 km s^{-1} in SN 2007if.

The 2003fg-like SNe with the fastest Si II velocities are consistent with the “shallow Silicon” (SS) SNe Ia from Folatelli et al. (2013). They are also consistent with the velocities of SN 1991T-like SNe (M. Phillips et al., in preparation). However, the lower velocities and early-time flatter Si II evolution are unusual compared to normal SNe Ia. In some cases, 2003fg-like SNe may have a very confined intermediate mass element layer in velocity space, and do not show a rapid drop in velocities at the earliest phases. This lack of an early drop may be caused by a compression of the Si shell, due to it running into an envelope (Quimby et al. 2006). In SNe Ia when the velocity measurements reach a minimum and stay at that value for a prolonged time, it usually requires the photosphere to pass through the base of the layer. By $+10 \text{ d}$ past maximum light the Si velocity is still declining. However, we note that features are susceptible to ionization changes and the bottom of the Si II layer does not always correspond to the bottom of the Si-region. Furthermore, the red side of the Si II feature becomes contaminated by Fe II lines after maximum light. For most 2003fg-like SNe this is after $+10 \text{ d}$ but for ASASSN-15hy this occurs 2-3 d past maximum (Lu et al. 2021). This can artificially produce a sudden velocity drop between 0 and $+10 \text{ d}$.

The velocities of the C II feature range between $10,000$ to $16,000 \text{ km s}^{-1}$ at -10 d to $8,000 \text{ km s}^{-1}$ at maximum light. For some of the 2003fg-like SNe (LSQ12gpw, SN 2012dn, and ASASSN-15hy) the velocity of the C II feature is lower than that of Si II. This may be an indication of mixing of the C and Si layers, or it may be a projected velocity effect where the Si II is located well above the photosphere, but the C II is located close to the photosphere, ensuring that most of the absorption is produced from material that is not directly moving towards the observer (Hoeflich 1990).

The top two panels and middle panel of Fig. 19 contain the pEW measurement of Si II $\lambda 5972$, $\lambda 6355$ and

C II $\lambda 6580$. The Si II $\lambda 6355$ feature slowly increases in pEW over time for all objects. At early times, around -10 d , the pEW of Si II $\lambda 6355$ ranges from $5\text{-}50 \text{ \AA}$, and rises to $20\text{-}90 \text{ \AA}$ by $+10 \text{ d}$. The pEW of the 2003fg-like SNe cover a larger range in values than 1991T-like SNe, which range from $0\text{-}20 \text{ \AA}$ at early times to $30\text{-}50 \text{ \AA}$ by $+10 \text{ d}$, and from shallow Si objects which cover a range of $0\text{-}50 \text{ \AA}$ at maximum light.

The pEW measurements of the Si II $\lambda 5972$ feature range from $0\text{-}10 \text{ \AA}$ at -10 d , to $10\text{-}30 \text{ \AA}$ at $+10 \text{ d}$ and follow a similar trend to Branch et al. (2006) SS SNe. Generally, the increasing pEW of this feature is interpreted as a cooling photosphere and the Si II $\lambda 5972$ line getting populated due to the recombination of Si III (e.g., Hachinger et al. 2008; Ashall et al. 2018).

The pEW of C II $\lambda 6580$ is more difficult to measure as it sits on the top of the re-emission of the Si II $\lambda 6355$ feature. The pEW decreases over time for all SNe, except SN 2006gz, SN 2013ao, CSS140501, and SN 2015M which have pEW values consistent with 0. The pEW measurements range from $5\text{-}20 \text{ \AA}$ at early times and $0\text{-}5 \text{ \AA}$ at $+10 \text{ d}$. Three of the 2003fg-like SNe (SN 2009dc, LSQ12gpw, and ASASSN-15hy) have persistent C II features well past maximum light. Interestingly, these SNe also have the slowest Si II $\lambda 6355$ velocities and the broadest light curves. These correlations will be discussed in more detail in the next section. Note that the pEW of C II $\lambda 6580$ region was measured even if no absorption feature was visible in the spectra, hence some SNe have values consistent with zero.

7. PARAMETER STUDY

Having measured and presented the main parameters of the 2003fg-like SNe, we now turn our attention to the correlations between these parameters and what these may imply about the physics of progenitors and explosion mechanisms. Fig. 20 presents six of the most significant correlations that were found within our data set, as well as two important non-correlations. For each correlation the least-squared best-fit line is given along with the 1-sigma uncertainty region. We show the Si II $\lambda 6355$ velocity and the C II pEW, both obtained within 3 days of B-maximum, t_{max}^{i-B} , the color $(B - V)$ at B-band maximum corrected only for Milky Way extinction, the color $(B_{max} - V_{max})$, and the B-band and pseudo-bolometric peak magnitude and flux corrected for host galaxy extinction. The p-value for each fit is provided above each panel.

Arguably the most interesting correlation is between the pEW of C II and the velocity of the Si II $\lambda 6355$, both taken at maximum light. SNe with slower Si II velocities tend to have larger values of C II pEW. Slower Si

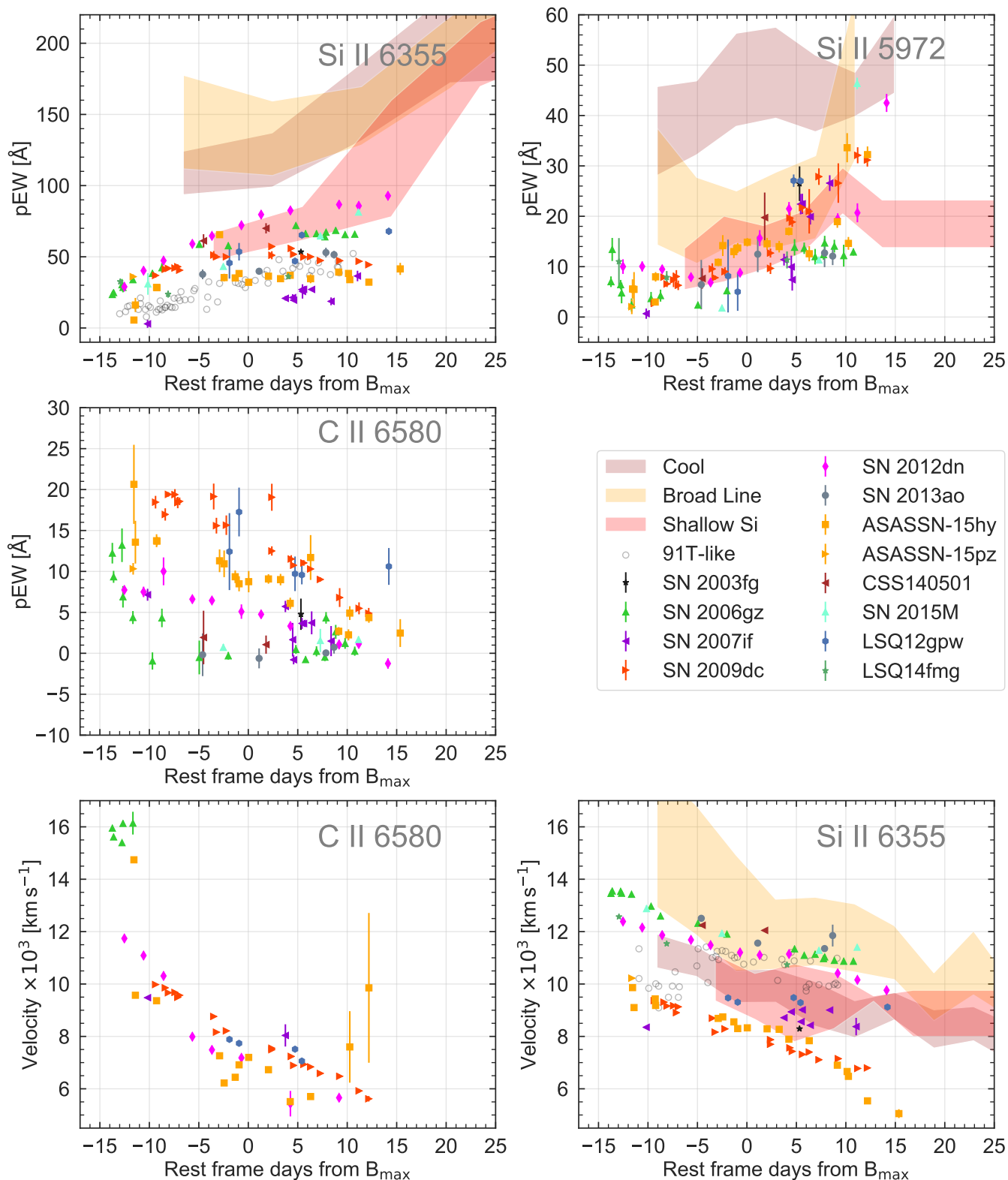


Figure 19. pEW and velocity measurements as a function of phase. *Top left:* Si II $\lambda 6355$ pEW as a function of phase relative to maximum. *Top right:* Si II $\lambda 5972$ pEW as a function of phase relative to maximum. *Middle left:* C II $\lambda 6580$ pEW as a function of phase from maximum. *Bottom left:* C II $\lambda 6580$ velocity as a function of phase relative to maximum. *Bottom right:* Si II $\lambda 6355$ velocity as a function of phase relative to maximum.

velocities could be produced by a WD exploding inside a carbon-rich envelope. The ejecta would slow down as they run into the envelope (Noebauer et al. 2016). In a simplistic picture, a large envelope mass would produce lower ejecta velocities, as more kinetic energy would be deposited into a more massive envelope. A larger envelope mass would also produce longer diffusion times and broader light curves, as is seen in the top middle panel of Fig. 20, where there is a correlation between C II pEW and $\Delta m_{15}(B)$. 2003fg-like SNe with broader light curves have larger C II features and slower Si II $\lambda 6355$ velocities. These three correlations point to a non-degenerate carbon-rich envelope as being the dominant cause of the observed diversity between 2003fg-like SNe. Interestingly, these correlations are not seen in normal SNe Ia, demonstrating that normal SN Ia are not produced via the envelope model. For example, faster declining SNe have the slowest ejecta velocities (e.g., Benetti et al. 2005; Gall et al. 2018; Ashall et al. 2018; Galbany et al. 2019).

The unique i -band behavior sets 2003fg-like SNe apart from other luminous events. 2003fg-like SNe generally show no secondary i -band maximum. The weak i -band secondary requires either full mixing in the ejecta or a lack of recombination of the Fe-group layers above the photosphere (Höflich et al. 2002; Kasen 2006; Jack et al. 2015). In the case of 2003fg-like SNe, the lack of an H -band break at +10 d indicates that the photosphere is not within the ^{56}Ni region and therefore the ejecta cannot be fully mixed. Instead, the weak i -band secondary maximum may be caused by a lack of recombination of Fe-group elements. The timing of the i -band maximum (t_{max}^{i-B})⁸ allows for 2003fg-like SNe to be distinguished from other SNe Ia (Ashall et al. 2020). 2003fg-like SNe with larger values of t_{max}^{i-B} tend to have lower values of Si II $\lambda 6355$ pEW . This is in contradiction with the trend seen between subluminal to normal SN Ia, where a lower value of t_{max}^{i-B} and stronger i -band secondary maximum are correlated with a higher ionization state and faster velocities (e.g., Kasen 2006). This is seen in 1991T-like SNe, but not in 2003fg-like SNe that show a weaker Si II $\lambda 6355$ pEW feature and larger values of t_{max}^{i-B} , possibly caused by longer diffusion timescales through the large carbon-rich outer envelope.

The t_{max}^{i-B} parameter is also found to be correlated with the observed ($B - V$) color at maximum light, and the difference between the B_{max} and V_{max} magnitudes (middle left and middle right panels of Fig. 20). In

both cases, the photometry was not corrected for host-galaxy extinction. Redder 2003fg-like SNe have larger values of t_{max}^{i-B} indicating cooler ejecta and a larger reprocessing of flux toward redder wavelengths. This is consistent with a homologous expansion which is adiabatically cooling. Line blanketing in the UV can also reprocess flux into redder wavelengths through fluorescence. It causes redder colors in SNe (Mazzali 2000; Lentz et al. 2000). As the line blanketing is due to the presence of heavy elements in the outer layers, differences in the magnitude of the line blanketing (resulting in differences in the UV-optical colors) could be caused by differences in the metallicity of the progenitor or the shape of the outer density profile (Walker et al. 2012). We note that the three correlations in the middle panels of Fig. 20 may be largely driven by ASASSN-15hy.

It should be noted, however, that there is no statistically significant correlation between the peak (B -band or bolometric) luminosity (both corrected and not corrected for host galaxy extinction) and the Si II velocity at maximum light. This is inconsistent with predictions from the super- M_{Ch} scenario (Howell et al. 2006). The lack of a correlation here implies that more than just the mass of the exploding WD drives the luminous display.

Overall the correlations in Fig. 20 are consistent with a degenerate core exploding inside a carbon-rich envelope. This could occur in the core-degenerate scenario. We discuss this further in Section 8.

8. DISCUSSION

Here we place into context our findings relative to three leading models of 2003fg-like SNe. One leading model consists of the disruption of a C-O WD that exceeds the M_{Ch} limit due to rapid rotation and/or high magnetic fields (Yoon & Langer 2005; Das & Mukhopadhyay 2013). Alternatively the merger of two WDs could produce SNe Ia exceeding the M_{Ch} -mass limit (e.g., Scalzo et al. 2010). Finally, another viable model may be the disruption of a C-O degenerate core within a dense circumstellar material environment (Hachinger et al. 2012; Noebauer et al. 2016). This is also referred to as an envelope model (Höflich & Khokhlov 1996). Such an explosion could be associated with an explosion of a degenerate core of an asymptotic giant branch (AGB) star (i.e. in the core degenerate scenario; Hsiao et al. 2020; Lu et al. 2021), or from a C-O WD explosion with surrounding circumstellar dust (Nagao et al. 2017, 2018). We discuss each of these models below.

8.1. Super- M_{Ch} WD

A single WD may exceed the M_{Ch} limit due to rapid rotation or high magnetic fields (Yoon & Langer 2005;

⁸ Note that in Fig. 20 t_{max}^{i-B} is obtained from the rest frame K-corrected data, whereas in Fig. 10 the data are not K-corrected to be consistent with the definition from Ashall et al. (2020).

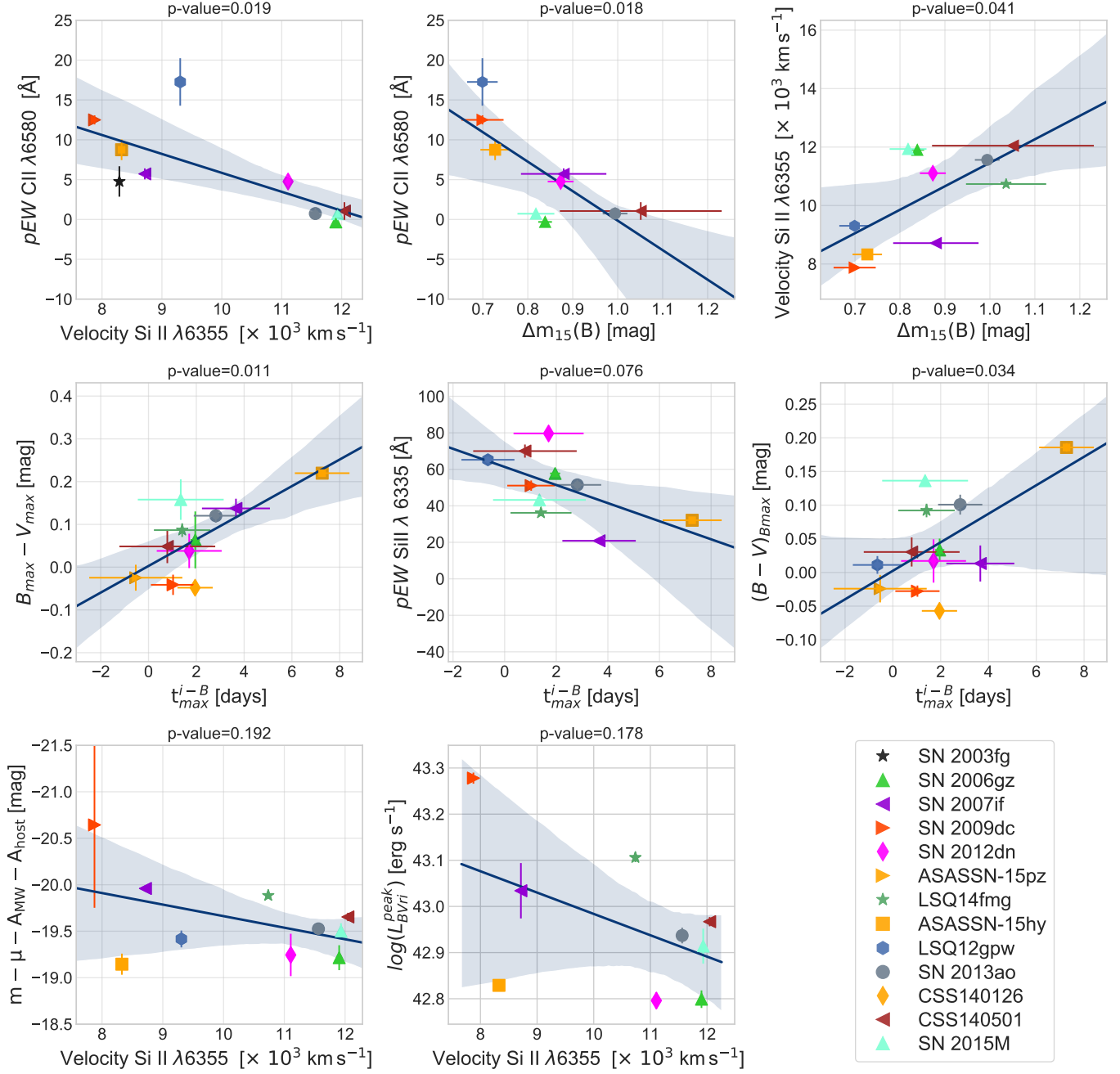


Figure 20. Correlation plots between measured parameters of 2003fg-like SNe. Above each panel the p-value is given. All relationships are statistically significant except for the lower left and lower middle panels between M_B , $L_{\text{BVri}}^{\text{peak}}$ and Si velocity. For each panel a line of best fit determined by a least-squares technique is provided along with a 1-sigma uncertainty shaded region. It should be noted that t_{max}^{i-B} in this plot has been K-corrected. A full pair-plot of all parameters can be found in Appendix B.

Das & Mukhopadhyay 2013). The mass limit of such models is thought to be $1.8M_{\odot}$ (Yoon & Langer 2005). A C/O WD exploding at such masses may be able to produce enough ^{56}Ni to power the extreme luminosities observed in some 2003fg-like SNe. However, due to this scenario requiring a detonation as the explosion mechanism, it has problems producing the large amounts of unburnt carbon, and intermediate mass elements, as well as the low ionization observed in the maximum light spectra (Hoeftlich & Khokhlov 1996).

In the Super- M_{Ch} WD scenario it was predicted that an increased total WD mass should result in a larger ^{56}Ni mass and a larger binding energy which would result in higher diffusion time scales, higher luminosities, lower kinetic energies, and lower ejecta velocities (Howell et al. 2006). However, in our sample there is no correlation between Si II $\lambda 6355$ velocity and peak B -band or bolometric magnitude⁹ (as a proxy for binding energy and ^{56}Ni mass), or between $\Delta m_{15}(B)$ and B -band or bolometric magnitude (both as a proxy for WD mass). Both of these correlations would be expected if the driving parameter amongst 2003fg-like SNe was ejecta mass. Furthermore, to produce the luminosity of the most luminous 2003fg-like SNe, such as SN 2003fg, requires an ejecta mass of $2.1M_{\odot}$ (Howell et al. 2006). This is above the mass limit ($1.8M_{\odot}$) of a single super Super- M_{Ch} WD (Yoon & Langer 2005).

8.2. Dynamically merging WDs

In the double-degenerate scenario, two WDs may dynamically merge and produce a large ^{56}Ni mass. The advantage of this scenario is that the total summed mass of the two WDs can exceed $1.8M_{\odot}$. The low levels of continuum polarization in the two 2003fg-like SNe that have data, SN 2007if and SN 2009dc (Tanaka et al. 2010; Cikota et al. 2019), make dynamical mergers an unlikely avenue to produce these 2003fg-like SNe, as such models are highly aspherical (Bulla et al. 2016). As there are many varieties of WD mass which may merge, as well as off center ^{56}Ni distributions from dynamical merger models, it would also be expected that dynamical mergers do not produce the correlations seen in the data.

8.3. Envelope model

The data and correlations presented in this work (Fig. 20) are consistent with the hydrogen (and possibly helium) free envelope model. In such model, a C/O WD explodes within a non-degenerate C-rich envelope (e.g., Hoeftlich & Khokhlov 1996). For a given WD mass, a

more massive envelope would produce stronger carbon lines, lower Si velocities, and longer diffusion time scales. This is evident in the correlations between Si II $\lambda 6355$ velocity and C II 6580\AA pEW (which is a proxy for envelope mass) and $\Delta m_{15}(B)$ (which is a proxy for diffusion time). The more massive carbon envelope would also produce the covering mass above the ^{56}Ni region which would naturally explain the observed very late onset of the H -band break. Furthermore, there are multiple factors affecting the luminosity. For a given WD mass, varying the envelope mass would produce a correlation between the expansion velocity and luminosity. In the case of a more massive envelope, the exploding WD would have more mass to deposit its energy into and decrease its speed, and this deposited energy would be converted into luminosity. Thus, both envelope mass and the ^{56}Ni mass contribute to the observed luminosity. Additional factors may be the flame propagation speed (e.g., deflagration or detonation) as discussed in Lu et al. (2021). Such a model may also be referred to as the deflagration-core-degenerate scenario. In the envelope scenario, reprocessing of the flux from the optical to NIR in the envelope would also produce the high NIR flux observed.

A viable progenitor scenario within the envelope model configuration is the core degenerate scenario. The core degenerate scenario is the explosion of the degenerate C/O core in the center of an AGB star. The signature of a superwind detected in the observations of LSQ14fmg provides a compelling link to an AGB progenitor (Hsiao et al. 2020). This class of models provides results which match the observational properties of both LSQ14fmg (Hsiao et al. 2020) and ASASSN-15hy (Lu et al. 2021).

Finally, in the core degenerate scenario there should be significant X-ray luminosity (Lu et al. 2021). This should be searched for in future nearby events. Another prediction of the core degenerate scenario is the formation of CO in the high-density and low-temperature non-degenerate envelope. It has been proposed that active CO formation manifests as the observed rapid decline in the optical light curve at various phases in SN 2009dc, SN 2012dn, LSQ14fmg, and CSS140126 (Hsiao et al. 2020). The timing of this drop is dictated by the envelope's ability to cool and is correlated with the envelope mass as indicated by the minimum of the Si II $\lambda 6355$ velocity (Quimby et al. 2006; Hsiao et al. 2020). Faster expanding ejecta cool faster. Another prediction from the core-degenerate scenario is an interaction with previous superwind episodes of the AGB star which may occur between 1 to 10 years after the SN explosion (Hsiao

⁹ Note that the distances to the 2003fg-like SNe are well determined and not the cause of this lack of correlation.

et al. 2020). Observationally this appear as a UV late time re-brightening (e.g., Graham et al. 2019).

One important parameter for core-degenerate models is low metallicity ($Z < Z_{\odot}^{-4}$) (Lu et al. 2021), which is also seen at the local environment of 2003fg-like SNe (Galbany et al. 2021). These low metallicities may come from population I or II stars. Contrary to normal SNe Ia, 2003fg-like SNe show no increase in UV flux ratio at early times. This is possibly caused by low metallicity of the progenitor and reduced line blanketing in the outer ejecta.

9. CONCLUSION

This paper presents a homogeneous sample of nine 2003fg-like SNe observed by the Carnegie Supernova Project I & II, which are analyzed in addition with 4 objects from the literature. This is the most complete 2003fg-like SNe dataset to date.

Photometrically not all 2003fg-like SNe are over-luminous. In fact in the optical (B and V bands), they populate the main part of the LWR with absolute B -band magnitudes between ~ -19 to ~ -21 mag. 2003fg-like SNe begin to differ from normal SNe Ia in the redder bands. In the i band, 2003fg-like SNe peak after time of B -band maximum and have weak secondary maxima. In the NIR bands, 2003fg-like SNe are unique and are at least 1 mag brighter than normal SNe Ia with the same optical light curve shape. Furthermore, their rise in the H band can be up to 40 d longer than in the B band.

Light-curve fitters determine that 2003fg-like SNe have negative Hubble residuals; i.e. they are too bright for their light curve shape. As 2003fg-like SNe preferentially explode in low mass, low metallicity and high specific star-forming galaxies they are more prevalent in the high-redshift universe. *Therefore, due to the similarity between normal and 2003fg-like SNe in the bluer bands (B & V), future high-redshift cosmological surveys should ensure they obtain rest-frame NIR observations in order to minimize bias introduced by the contamination of 2003fg-like SNe.* As this may not always be possible, it is important to carefully study 2003fg-like SNe to fully understand the bias they will cause in SN cosmology.

Optical spectra of 2003fg-like SNe are similar to that of normal SNe Ia, but most have strong carbon absorption well past maximum light, as well as low velocity gradients before maximum light. In the NIR, 2003fg-like SNe do not show a distinct H -band break at ~ 10 d. In 2003fg-like SNe, this H -band break is not visible until beyond 70 d past maximum light.

With our large sample of 2003fg-like SNe we find that the ubiquitous characteristics of all 2003fg-like SNe are:

- A broad optical light curve shape ($\Delta m_{15}(B) < 1.3$ mag).
- The primary i -band peaks after the phase of B -band maximum.
- A lack of strong Fe III features in the early spectra
- A peak H -band absolute magnitude brighter than -19 mag.
- Carbon absorption at early times (-10 d from maximum light).
- No clear H -band break at $+10$ d from maximum light.

These criteria should be used in future studies to determine if a SN is truly 2003fg-like.

In 2003fg-like SNe the luminous long-rising NIR light curves may be caused by the reprocessing of flux to the NIR as the result of an explosion inside a massive envelope. The lack of an early H -band break also demonstrates that the photosphere is not within the ^{56}Ni region until a much later epoch. These observations provide direct evidence that there is a significant amount of ejecta above the ^{56}Ni region.

A number of unique and interesting correlations were found within our dataset. There are strong correlations between the pEW of the C II feature at maximum light, the Si II velocity at maximum light, and $\Delta m_{15}(B)$. 2003fg-like SNe with larger C II pEWs have slower Si II velocities at maximum light and broader light curves. These correlations are fully consistent with an envelope model where a C/O degenerate star explodes within an envelope. In such a configuration for a given degenerate core mass a larger envelope mass would produce slower Si velocities and larger diffusion time scales. Given that there are no H or He lines in 2003fg-like SNe spectra it is likely that this envelope is carbon/oxygen dominated. One promising progenitor scenario and explosion mechanism is the core degenerate scenario (Kashi & Soker 2011; Hsiao et al. 2020; Lu et al. 2021).

The data presented here provide a new critical piece of information in determining the source of diversity of 2003fg-like SNe and the nature of SNe Ia in general. It is clear that 2003fg-like SNe are far more diverse than previously thought. Only with high-precision observations extending from optical through NIR wavelengths can the physics be clearly understood. It is apparent that simply changing the mass of the exploding WD will not produce all of the observational characteristics.

Our data are consistent with a degenerate core exploding within a carbon-rich envelope, with the core degenerate scenario providing one of the strongest paths to produce 2003fg-like SN events.

The authors would like to thank Vanessa Díaz for helping with data visualization. CA and BJS are supported by NASA grant 80NSSC19K1717 and NSF grants AST-1920392 and AST-1911074. M.S. and F.T. are supported by grants from the Villum FONDEN (28021) and the Independent Research Fund Denmark (8021-00170B). E.B. was supported in part by NASA grant 80NSSC20K0538. N.B.S. acknowledges support from the Texas A&M University Mitchell/Heep/Munnerlyn Chair in Observational Astronomy. L.G. was funded by the European Union’s Horizon 2020 research and innovation programme under the Marie Skłodowska-Curie grant agreement No. 839090. The CSP has been funded by the NSF under grants AST-0306969, AST-0607438, AST-1008343, AST-1613426, AST-1613455, and AST-1613472, and in part by a Sapere Aude Level 2 grant funded by the Danish Agency for Science and Technology and Innovation (PI M.S.). Time domain research by D.J.S. is supported by NSF grants AST-1821987, 1813466, & 1908972, and by the Heising-Simons Foundation under grant #2020-1864. Based on observations made with the Nordic Optical Telescope, owned in collaboration by the University of Turku and Aarhus University, and operated jointly by Aarhus University, the University of Turku and the University of Oslo, representing Denmark, Finland and Norway, the University of Iceland and Stockholm University at the Observatorio del Roque de los Muchachos, La Palma, Spain, of the Instituto de Astrofísica de Canarias.

Facilities: : Magellan, du Pont, Swope, Nordic Optical Telescope

Software: IRAF (Tody 1986, 1993), SNooPy (Burns et al. 2011), Astropy (Astropy Collaboration et al. 2013, 2018), IDL Astronomy user’s library (Landsman 1995) and misfits (S. Holmbo et al., in prep.).

REFERENCES

- Akerlof, C., Miller, J., Peters, C., et al. 2007, Central Bureau Electronic Telegrams, 1059, 2
- Ashall, C., Mazzali, P. A., Pian, E., & James, P. A. 2016, MNRAS, 463, 1891
- Ashall, C., Mazzali, P. A., Stritzinger, M. D., et al. 2018, MNRAS, 477, 153
- Ashall, C., Hsiao, E. Y., Hoefflich, P., et al. 2019a, ApJL, 875, L14
- Ashall, C., Hoefflich, P., Hsiao, E. Y., et al. 2019b, ApJ, 878, 86
- Ashall, C., Lu, J., Burns, C., et al. 2020, ApJL, 895, L3
- Astropy Collaboration, Robitaille, T. P., Tollerud, E. J., et al. 2013, A&A, 558, A33
- Astropy Collaboration, Price-Whelan, A. M., Sipőcz, B. M., et al. 2018, AJ, 156, 123
- Baltay, C., Rabinowitz, D., Hadjijska, E., et al. 2013a, PASP, 125, 683
- . 2013b, PASP, 125, 683
- Benetti, S., Cappellaro, E., Mazzali, P. A., et al. 2005, ApJ, 623, 1011
- Benitez, S., Polshaw, J., Inserra, C., et al. 2014, The Astronomer’s Telegram, 6118, 1
- Blondin, S., Matheson, T., Kirshner, R. P., et al. 2012, AJ, 143, 126
- Bock, G., Parrent, J. T., & Howell, D. A. 2012, Central Bureau Electronic Telegrams, 3174, 1
- Branch, D., Dang, L. C., Hall, N., et al. 2006, PASP, 118, 560
- Brimacombe, J., Marples, P., Kiyota, S., et al. 2015, The Astronomer’s Telegram, 8099, 1
- Brown, P. J., Breeveld, A. A., Holland, S., Kuin, P., & Pritchard, T. 2014a, Ap&SS, 354, 89
- Brown, P. J., Kuin, P., Scalzo, R., et al. 2014b, ApJ, 787, 29
- Bulla, M., Sim, S. A., Pakmor, R., et al. 2016, MNRAS, 455, 1060
- Burns, C. R., Stritzinger, M., Phillips, M. M., et al. 2011, AJ, 141, 19
- . 2014, ApJ, 789, 32
- Burns, C. R., Parent, E., Phillips, M. M., et al. 2018, ApJ, 869, 56
- Burrow, A., Baron, E., Ashall, C., et al. 2020, ApJ, 901, 154
- Cappellaro, E., Patat, F., Mazzali, P. A., et al. 2001, ApJL, 549, L215
- Chakradhari, N. K., Sahu, D. K., Srivastav, S., & Anupama, G. C. 2014, MNRAS, 443, 1663
- Chen, P., Dong, S., Katz, B., et al. 2019, ApJ, 880, 35
- Childress, M., Aldering, G., Aragon, C., et al. 2011, ApJ, 733, 3
- Cikota, A., Patat, F., Wang, L., et al. 2019, MNRAS, 490, 578
- Das, U., & Mukhopadhyay, B. 2013, PhRvL, 110, 071102
- Dessart, L., Hillier, D. J., Blondin, S., & Khokhlov, A. 2014, MNRAS, 439, 3114
- Drake, A. J., Djorgovski, S. G., Mahabal, A., et al. 2009, ApJ, 696, 870
- Drake, A. J., Djorgovski, S. G., Graham, M. J., et al. 2013a, Central Bureau Electronic Telegrams, 3442, 1
- . 2013b, Central Bureau Electronic Telegrams, 3442, 1
- Filippenko, A. V., Richmond, M. W., Branch, D., et al. 1992a, AJ, 104, 1543
- Filippenko, A. V., Richmond, M. W., Matheson, T., et al. 1992b, ApJL, 384, L15
- Firth, R. E., Sullivan, M., Gal-Yam, A., et al. 2015, MNRAS, 446, 3895
- Fleury, M., Leget, P. F., Le Guillou, L., et al. 2014, The Astronomer’s Telegram, 5720, 1
- Folatelli, G., Morrell, N., Phillips, M. M., et al. 2013, ApJ, 773, 53
- Foley, R. J., Narayan, G., Challis, P. J., et al. 2010, ApJ, 708, 1748
- Foley, R. J., Challis, P. J., Chornock, R., et al. 2013, ApJ, 767, 57
- Galbany, L., Ashall, C., Höflich, P., et al. 2019, A&A, 630, A76
- Galbany, L., et al. 2021, ApJ, submitted
- Gall, C., Stritzinger, M. D., Ashall, C., et al. 2018, A&A, 611, A58
- Ganeshalingam, M., Li, W., Filippenko, A. V., et al. 2012, ApJ, 751, 142
- Garavini, G., Folatelli, G., Nobili, S., et al. 2007, A&A, 470, 411
- González-Gaitán, S., Hsiao, E. Y., Pignata, G., et al. 2014, ApJ, 795, 142
- Graham, M. L., Kumar, S., Hosseinzadeh, G., et al. 2017, MNRAS, 472, 3437
- Graham, M. L., Harris, C. E., Nugent, P. E., et al. 2019, ApJ, 871, 62
- Hachinger, S., Mazzali, P. A., Tanaka, M., Hillebrandt, W., & Benetti, S. 2008, MNRAS, 389, 1087
- Hachinger, S., Mazzali, P. A., Taubenberger, S., et al. 2012, MNRAS, 427, 2057
- Hammer, D., Verdoes Kleijn, G., Hoyos, C., et al. 2010, ApJS, 191, 143
- Hamuy, M., Folatelli, G., Morrell, N. I., et al. 2006, PASP, 118, 2
- Hicken, M., Garnavich, P. M., Prieto, J. L., et al. 2007, ApJL, 669, L17

- Hoeflich, P. 1990, *A&A*, 229, 191
- Hoeflich, P., & Khokhlov, A. 1996, *ApJ*, 457, 500
- Höflich, P., Gerardy, C. L., Fesen, R. A., & Sakai, S. 2002, *ApJ*, 568, 791
- Holoien, T. W. S., Stanek, K. Z., Kochanek, C. S., et al. 2015, *The Astronomer's Telegram*, 7450, 1
- Howell, D. A., Sullivan, M., Nugent, P. E., et al. 2006, *Nature*, 443, 308
- Hsiao, E. Y., Conley, A., Howell, D. A., et al. 2007, *ApJ*, 663, 1187
- Hsiao, E. Y., Marion, G. H., Phillips, M. M., et al. 2013, *ApJ*, 766, 72
- Hsiao, E. Y., Burns, C. R., Contreras, C., et al. 2015, *A&A*, 578, A9
- Hsiao, E. Y., Phillips, M. M., Marion, G. H., et al. 2019, *PASP*, 131, 014002
- Hsiao, E. Y., Hoeflich, P., Ashall, C., et al. 2020, *ApJ*, 900, 140
- Iben, I., J., & Tutukov, A. V. 1984, *ApJS*, 54, 335
- Inserra, C., Nicholl, M., Walton, N., et al. 2013, *The Astronomer's Telegram*, 4863, 1
- Jack, D., Baron, E., & Hauschildt, P. H. 2015, *MNRAS*, 449, 3581
- Jiang, J.-a., Doi, M., Maeda, K., & Shigeyama, T. 2018, *ApJ*, 865, 149
- Kasen, D. 2006, *ApJ*, 649, 939
- Kashi, A., & Soker, N. 2011, *MNRAS*, 417, 1466
- Kirshner, R. P., Willner, S. P., Becklin, E. E., Neugebauer, G., & Oke, J. B. 1973, *ApJL*, 180, L97
- Kochanek, C. S., Shappee, B. J., Stanek, K. Z., et al. 2017, *PASP*, 129, 104502
- Krisciunas, K., Contreras, C., Burns, C. R., et al. 2017, *AJ*, 154, 211
- Kromer, M., Ohlmann, S. T., Pakmor, R., et al. 2015, *MNRAS*, 450, 3045
- Landsman, W. B. 1995, in *Astronomical Society of the Pacific Conference Series*, Vol. 77, *Astronomical Data Analysis Software and Systems IV*, ed. R. A. Shaw, H. E. Payne, & J. J. E. Hayes, 437
- Leibundgut, B., Kirshner, R. P., Phillips, M. M., et al. 1993, *AJ*, 105, 301
- Lentz, E. J., Baron, E., Branch, D., Hauschildt, P. H., & Nugent, P. E. 2000, *ApJ*, 530, 966
- Li, W., Filippenko, A. V., Chornock, R., et al. 2003, *PASP*, 115, 453
- Lira, P., Suntzeff, N. B., Phillips, M. M., et al. 1998, *AJ*, 115, 234
- Livne, E. 1990, *ApJL*, 354, L53
- Lu, J., et al. 2021, *ApJ*, submitted
- Maeda, K., Kawabata, K., Li, W., et al. 2009, *ApJ*, 690, 1745
- Maguire, K., Pan, Y., Le Guillou, L., et al. 2012, *The Astronomer's Telegram*, 4644, 1
- Marion, G. H., Höflich, P., Gerardy, C. L., et al. 2009, *AJ*, 138, 727
- Masci, F. J., Laher, R. R., Rebbapragada, U. D., et al. 2017, *PASP*, 129, 014002
- Mazzali, P. A. 2000, *A&A*, 363, 705
- Mazzali, P. A., & Hachinger, S. 2012, *MNRAS*, 424, 2926
- Mazzali, P. A., Sauer, D. N., Pastorello, A., Benetti, S., & Hillebrandt, W. 2008, *MNRAS*, 386, 1897
- Mazzali, P. A., Sullivan, M., Hachinger, S., et al. 2014, *MNRAS*, 439, 1959
- Morokuma, T., Tominaga, N., Tanaka, M., et al. 2014, *PASJ*, 66, 114
- Morokuma, T., Mazzali, P., Piascik, A., et al. 2015, *The Astronomer's Telegram*, 7532, 1
- Mould, J. R., Huchra, J. P., Freedman, W. L., et al. 2000, *ApJ*, 529, 786
- Nagao, T., Maeda, K., & Yamanaka, M. 2017, *ApJ*, 835, 143
- . 2018, *MNRAS*, 476, 4806
- Noebauer, U. M., Taubenberger, S., Blinnikov, S., Sorokina, E., & Hillebrandt, W. 2016, *MNRAS*, 463, 2972
- Parrent, J. T., Howell, D. A., Fesen, R. A., et al. 2016, *MNRAS*, 457, 3702
- Perlmutter, S., Aldering, G., Goldhaber, G., et al. 1999, *ApJ*, 517, 565
- Phillips, M. M. 1993, *ApJL*, 413, L105
- Phillips, M. M., Lira, P., Suntzeff, N. B., et al. 1999, *AJ*, 118, 1766
- Phillips, M. M., Wells, L. A., Suntzeff, N. B., et al. 1992, *AJ*, 103, 1632
- Phillips, M. M., Phillips, A. C., Heathcote, S. R., et al. 1987, *PASP*, 99, 592
- Phillips, M. M., Simon, J. D., Morrell, N., et al. 2013, *ApJ*, 779, 38
- Phillips, M. M., Contreras, C., Hsiao, E. Y., et al. 2019, *PASP*, 131, 014001
- Poznanski, D., Prochaska, J. X., & Bloom, J. S. 2012, *MNRAS*, 426, 1465
- Pskovskii, Y. P. 1984, *Soviet Ast.*, 28, 658
- Puckett, T., Moore, R., Newton, J., & Orff, T. 2009, *Central Bureau Electronic Telegrams*, 1762, 1
- Puckett, T., & Pelloni, A. 2006, *IAUC*, 8754, 2
- Quimby, R., Höflich, P., Kannappan, S. J., et al. 2006, *ApJ*, 636, 400
- Riess, A. G., Filippenko, A. V., Challis, P., et al. 1998, *AJ*, 116, 1009

- Scalzo, R. A., Ruiter, A. J., & Sim, S. A. 2014, *MNRAS*, 445, 2535
- Scalzo, R. A., Aldering, G., Antilogus, P., et al. 2010, *ApJ*, 713, 1073
- Schlafly, E. F., & Finkbeiner, D. P. 2011, *ApJ*, 737, 103
- Shappee, B. J., Prieto, J. L., Grupe, D., et al. 2014, *ApJ*, 788, 48
- Silverman, J. M., Ganeshalingam, M., Li, W., et al. 2011, *MNRAS*, 410, 585
- Simcoe, R. A., Burgasser, A. J., Schechter, P. L., et al. 2013, *PASP*, 125, 270
- Smartt, S. J., Valenti, S., Fraser, M., et al. 2015, *A&A*, 579, A40
- Stritzinger, M. D., Valenti, S., Hoefflich, P., et al. 2015, *A&A*, 573, A2
- Tanaka, M., Kawabata, K. S., Yamanaka, M., et al. 2010, *ApJ*, 714, 1209
- Taubenberger, S., Kromer, M., Pakmor, R., et al. 2013a, *ApJL*, 775, L43
- Taubenberger, S., Benetti, S., Childress, M., et al. 2011, *MNRAS*, 412, 2735
- Taubenberger, S., Kromer, M., Hachinger, S., et al. 2013b, *MNRAS*, 432, 3117
- Taubenberger, S., Floers, A., Vogl, C., et al. 2019, *MNRAS*, 488, 5473
- Tody, D. 1986, in *Society of Photo-Optical Instrumentation Engineers (SPIE) Conference Series*, Vol. 627, *Instrumentation in astronomy VI*, ed. D. L. Crawford, 733
- Tody, D. 1993, in *Astronomical Society of the Pacific Conference Series*, Vol. 52, *Astronomical Data Analysis Software and Systems II*, ed. R. J. Hanisch, R. J. V. Brissenden, & J. Barnes, 173
- Walker, E. S., Hachinger, S., Mazzali, P. A., et al. 2012, *MNRAS*, 427, 103
- Walker, E. S., Baltay, C., Campillay, A., et al. 2015, *ApJS*, 219, 13
- Wheeler, J. C., Höfflich, P., Harkness, R. P., & Spyromilio, J. 1998, *ApJ*, 496, 908
- Whelan, J., & Iben, Icko, J. 1973, *ApJ*, 186, 1007
- Yamanaka, M., Kawabata, K. S., Kinugasa, K., et al. 2009, *ApJL*, 707, L118
- Yoon, S. C., & Langer, N. 2005, *A&A*, 435, 967
- Yuan, F., Quimby, R. M., Wheeler, J. C., et al. 2010, *ApJ*, 715, 1338
- Zhang, J.-J., Wang, X.-F., Sasdelli, M., et al. 2016, *ApJ*, 817, 114

APPENDIX

A. OBSERVATIONAL DETAILS

A.1. *Discovery Information*

The discovery information of the five 2003fg-like SNe with CSP-II data that are not previously published is outlined here:

LSQ12gpw was discovered by the La Silla-QUEST Low Redshift Supernova Survey (LSQ; Baltay et al. 2013b). The earliest images where the object is present were obtained on 2012 November 16.1 and 16.2 UT yielding 20.9 and 20.8 mag, respectively. The image of last non-detection was taken on 2012 November 14.2 UT with a limiting magnitude of 21.5 mag. The classification spectrum was taken on 2012 December 6.25 UT with EFOSC2 on the ESO New Technology Telescope as part of the Public ESO Spectroscopic Survey for Transient Objects (PESSTO; Smartt et al. 2015). The spectrum resembles that of SN 2006gz (Maguire et al. 2012). The rising light curves of LSQ12gpw have been examined in detail by Firth et al. (2015) and Jiang et al. (2018). The Swope light curves have also been published by Walker et al. (2015). Here, we present the same dataset but calibrated using the procedures outlined in Phillips et al. (2019).

SN 2013ao was discovered by the Catalina Real-Time Transient Survey (CRTS; Drake et al. 2009) and was originally designated CSS130315:114445-203140 and SSS130304:114445-203141. The SN was discovered in an image taken on 2013 March 4.77 UT yielding a discovery magnitude of 17.0 mag. There is no strong constraint on the explosion date from CRTS as the previous image of the object was taken more than 8 months prior (Drake et al. 2013b). The classification spectrum was taken on 2013 March 6.21 UT by PESSTO and resembles that of pre-maximum normal SNe Ia (Inserra et al. 2013).

CSS140126:120307-010132 or CSS140126 for short was also discovered by CRTS using multiple images obtained on 2014 January 2.5 UT, yielding a discovery magnitude of 18.8 mag. There is no strong constraint on the explosion date from CRTS as the previous image of the object was taken more than 6 months prior. The classification spectrum was taken on 2014 January 4.32 UT by PESSTO and resembles that of 1991T-like SNe Ia (Fleury et al. 2014).

CSS140501:170414+174839 or CSS140501 for short was also discovered by the CRTS using multiple images obtained on 2014 May 1.5 UT, yielding a discovery magnitude of 18.7 mag. The SN is also present in multiple images taken on 2014 April 23.5 UT, corresponding to -16.7 d relative to B -band maximum, at 19.7 mag. The last non-detection is based on multiple images taken on 2014 April 7.5 UT with a limiting magnitude of 20.7 mag. The classification spectrum was taken on 2014 May 5.32 UT by PESSTO and was reported to match the spectra of several SNe Ia before maximum light (Benitez et al. 2014).

SN 2015M (KISS15n) was discovered by the Kiso Supernova Survey (KISS; Morokuma et al. 2014) using an image obtained on 2015 May 10.54 UT yielding a discovery magnitude of $g = 18.3$ mag. No transient was detected in an image observed by the Intermediate Palomar Transient Factory (Masci et al. 2017) on 2015 May 6.30 UT with a limiting magnitude of $g = 19.4$ mag. ASAS-SN (Shappee et al. 2014; Kochanek et al. 2017) provides an additional non-detection on 2015 May 7.44 UT with a limiting magnitude of $V = 16.85$ mag. Two classification spectra were obtained using the SPRAT instrument on the Liverpool Telescope on 2015 May 17.08 UT and the Andalucia Faint Object Spectrograph and Camera on the Nordic Optical Telescope on 2015 May 16.12 UT. Both spectra resemble those of pre-maximum 1991T-like objects (Morokuma et al. 2015). While the object is located toward the Coma Cluster, it is unclear whether it is a cluster member. The supernova redshift from the classification spectra is roughly consistent with that of the Coma Cluster. Images obtained using the Advanced Camera for Surveys (ACS) on the Hubble Space Telescope as part of the ACS Coma Cluster Treasury Survey show the presumed host galaxy at the position of the SN (COMAi13032.301p275841.02; Hammer et al. 2010).

A.2. *CSP Photometry and Spectroscopy*

The photometry of LSQ12gpw, SN 2013ao, CSS140126, CSS140501 and SN 2015M is tabulated in Table A1, A2, A3, A4 and A5 respectively. Together with four previously published 2003fg-like SNe followed by CSP-I and CSP-II, the light curves are plotted individually in Fig. A1. All magnitudes are presented in the CSP natural system and have not been K- or S-corrected.

Twenty-four optical and six NIR spectroscopic observations of nine 2003fg-like SNe were obtained by the CSP I & II. The log of these unpublished CSP spectra can be seen in Table A6.

B. CORRELATIONS

In Fig. B1, pair plots of all the parameters previously shown in the text is presented. Section 7 highlights the ones have significant correlations.

Table A1. CSP natural system photometry for LSQ12gpw.

MJD	Phase ^a	<i>B</i>	<i>V</i>	<i>r</i>	<i>i</i>
Days	Days	Mag	Mag	Mag	Mag
56268.2	−1.0	17.60(0.01)	17.45(0.02)	17.48(0.02)	17.85(0.03)
56269.3	0.0	17.62(0.01)	17.48(0.02)	17.50(0.02)	17.90(0.03)
56270.2	0.9	17.61(0.02)	17.46(0.02)	17.48(0.02)	17.86(0.03)
56271.2	1.9	17.63(0.02)	17.46(0.02)	17.47(0.03)	17.85(0.04)
56272.2	2.8	17.63(0.02)	17.47(0.02)	17.51(0.02)	17.89(0.03)
56273.2	3.8	17.65(0.02)	17.49(0.02)	17.53(0.03)	17.90(0.03)
56274.1	4.6	17.70(0.02)	17.49(0.02)	17.54(0.03)	17.93(0.03)
56275.2	5.7	17.74(0.02)	17.52(0.02)	17.54(0.03)	17.92(0.04)
56276.2	6.6	17.76(0.02)	17.54(0.02)	17.58(0.03)	17.97(0.03)
56277.2	7.6	17.82(0.02)	17.59(0.02)	17.60(0.03)	18.02(0.03)
56282.2	12.3	18.14(0.02)	17.74(0.02)	17.77(0.02)	18.08(0.03)
56288.2	18.0	18.62(0.03)	18.03(0.03)	17.91(0.02)	18.16(0.03)

^aRest frame days relative to the time of *B*-band maximum given in Table 2.

Table A2. CSP natural system photometry for SN 2013ao.

MJD	Phase ^a	<i>u</i>	<i>B</i>	<i>g</i>	<i>V</i>	<i>r</i>	<i>i</i>	<i>Y</i>	<i>J</i>	<i>H</i>
Days	Days	Mag	Mag	Mag	Mag	Mag	Mag	Mag	Mag	Mag
56358.3	−3.6	17.29(0.02)	17.05(0.01)	16.93(0.01)	17.02(0.02)	16.99(0.01)	17.21(0.01)
56359.3	−2.6	16.89(0.01)	...	16.93(0.01)
56360.3	−1.7	17.33(0.02)	16.97(0.02)	16.88(0.01)	16.94(0.03)	16.90(0.01)	17.16(0.01)
56364.3	2.2	17.54(0.02)	16.98(0.01)	16.87(0.01)	16.89(0.01)	16.80(0.01)	17.11(0.01)
56365.2	3.0	17.63(0.02)	17.03(0.02)	16.89(0.01)	16.86(0.03)	16.80(0.01)	17.12(0.01)
56366.2	4.0	17.72(0.02)	17.09(0.01)	16.92(0.01)	16.89(0.01)	16.79(0.01)	17.09(0.01)
56367.2	5.0	17.80(0.02)	17.12(0.01)	16.95(0.01)	16.91(0.01)	16.80(0.01)	17.11(0.01)
56368.2	5.9	17.92(0.01)	17.17(0.01)	17.00(0.01)	16.93(0.01)	16.80(0.01)	17.14(0.01)
56369.2	6.9	18.00(0.02)	...	17.04(0.01)	...	16.81(0.01)	17.11(0.01)
56370.3	7.9	18.15(0.02)	17.30(0.02)	17.10(0.01)	16.95(0.03)	16.82(0.01)	17.15(0.01)
56371.2	8.8	18.24(0.02)	17.40(0.01)	17.17(0.01)	17.02(0.01)	16.84(0.01)	17.17(0.01)
56372.2	9.8	18.39(0.02)	17.47(0.02)	17.24(0.01)	17.04(0.01)	16.86(0.01)	17.18(0.01)
56373.2	10.7	18.50(0.02)	17.58(0.01)	17.32(0.01)	17.09(0.01)	16.88(0.01)	17.20(0.01)
56374.2	11.7	18.60(0.02)	17.65(0.01)	17.38(0.01)	17.12(0.01)	16.90(0.01)	17.23(0.01)
56375.2	12.6	18.78(0.02)	17.74(0.02)	17.47(0.01)	17.17(0.03)	16.93(0.02)	17.23(0.02)	17.17(0.02)	17.41(0.02)	17.13(0.04)

Table A2 continued

Table A2 (continued)

MJD	Phase ^a	<i>u</i>	<i>B</i>	<i>g</i>	<i>V</i>	<i>r</i>	<i>i</i>	<i>Y</i>	<i>J</i>	<i>H</i>
Days	Days	Mag	Mag	Mag	Mag	Mag	Mag	Mag	Mag	Mag
56376.2	13.6	18.94(0.03)	17.87(0.02)	17.56(0.01)	17.24(0.02)	16.97(0.01)	17.27(0.01)	17.15(0.01)	17.45(0.04)	...
56377.2	14.5	17.14(0.01)	17.46(0.03)	...
56378.2	15.5	17.10(0.01)	17.49(0.03)	...
56379.2	16.6	19.34(0.06)	18.24(0.03)	17.84(0.02)	17.40(0.04)	17.05(0.01)	17.32(0.02)	17.04(0.01)	17.51(0.03)	17.13(0.04)
56380.2	17.4	19.48(0.04)	18.33(0.02)	17.94(0.02)	17.50(0.03)	17.12(0.01)	17.35(0.02)
56381.2	18.4	19.55(0.04)	18.40(0.02)	18.01(0.01)	17.54(0.03)	17.15(0.02)	17.37(0.02)
56382.1	19.2	19.64(0.04)	18.53(0.02)	18.12(0.01)	17.59(0.01)	17.20(0.01)	17.38(0.01)
56383.2	20.3	19.83(0.04)	18.62(0.02)	18.21(0.01)	17.67(0.02)	17.24(0.01)	17.38(0.01)
56384.2	21.2	19.91(0.04)	18.74(0.02)	18.30(0.01)	17.72(0.01)	17.26(0.01)	17.38(0.01)	16.98(0.01)	17.48(0.04)	17.11(0.04)
56385.2	22.2	20.07(0.03)	18.79(0.02)	18.39(0.01)	17.79(0.02)	17.32(0.01)	17.41(0.01)
56386.1	23.1	20.08(0.03)	18.89(0.02)	18.45(0.01)	17.83(0.01)	17.35(0.01)	17.40(0.01)
56387.1	24.0	...	18.92(0.02)	18.53(0.01)	17.91(0.01)	17.38(0.01)	17.42(0.01)
56388.2	25.1	20.20(0.03)	19.05(0.02)	18.60(0.01)	17.93(0.03)	17.42(0.01)	17.43(0.01)
56389.2	26.0	20.30(0.04)	19.12(0.02)	18.66(0.01)	17.99(0.02)	17.46(0.01)	17.48(0.01)
56390.1	26.9	...	19.14(0.02)	18.71(0.01)	18.00(0.03)	17.48(0.01)	17.46(0.02)
56391.2	28.0	20.34(0.05)	19.21(0.02)	18.77(0.01)	18.08(0.01)	17.54(0.01)	17.51(0.01)
56393.2	29.8	20.59(0.07)	19.31(0.04)	18.88(0.02)	18.17(0.02)	17.61(0.01)	17.56(0.01)
56397.2	33.7	20.74(0.05)	19.49(0.03)	19.02(0.02)	18.35(0.02)	17.75(0.01)	17.68(0.02)
56398.1	34.6	20.64(0.06)	19.53(0.02)	19.06(0.01)	18.37(0.02)	17.79(0.01)	17.74(0.01)
56399.1	35.5	...	19.57(0.02)	19.10(0.01)	18.42(0.02)	17.82(0.01)	17.76(0.01)	16.95(0.01)	17.56(0.03)	17.24(0.04)
56400.1	36.5	...	19.54(0.02)	19.11(0.01)	18.44(0.02)	17.87(0.01)	17.80(0.01)
56401.0	37.3	...	19.53(0.03)	19.13(0.02)	18.44(0.03)	17.88(0.01)	17.81(0.02)
56402.2	38.4	...	19.66(0.04)	19.18(0.02)	18.49(0.03)	17.94(0.01)	17.85(0.01)
56403.0	39.3	...	19.62(0.04)	19.20(0.02)	18.50(0.02)	17.96(0.02)	17.88(0.02)
56404.0	40.2	21.01(0.16)	19.58(0.04)	19.24(0.02)	18.52(0.02)	18.00(0.01)	17.94(0.02)
56407.2	43.3	...	19.68(0.08)	19.33(0.04)	18.63(0.03)	18.12(0.02)	18.05(0.02)
56409.2	45.2	...	19.83(0.15)	19.36(0.05)	18.06(0.02)
56410.1	46.1	...	19.76(0.05)	19.31(0.02)	18.77(0.02)	18.20(0.01)	18.16(0.01)
56411.2	47.0	...	19.78(0.04)	19.38(0.02)	18.75(0.02)	18.25(0.01)	18.20(0.01)
56415.2	51.0	...	19.92(0.04)	19.46(0.02)	18.85(0.02)	18.36(0.01)
56416.2	51.8	21.04(0.07)	19.83(0.03)	19.48(0.01)	18.87(0.03)	18.38(0.01)	18.40(0.02)
56417.1	52.8	21.07(0.07)	19.94(0.02)	19.47(0.01)	18.86(0.03)	18.41(0.01)	18.43(0.01)
56418.2	53.8	21.14(0.08)	19.95(0.02)	19.51(0.01)	18.90(0.03)	18.44(0.01)	18.49(0.02)
56419.2	54.8	...	19.94(0.02)	19.51(0.01)	18.94(0.02)	18.45(0.01)	18.52(0.01)
56420.2	55.7	21.14(0.07)	19.96(0.03)	19.55(0.01)	18.95(0.03)	18.48(0.02)	18.54(0.02)
56422.2	57.7	19.56(0.02)	...	18.53(0.01)	18.58(0.01)
56423.2	58.6	...	20.02(0.03)	...	18.98(0.03)	18.56(0.01)	18.63(0.02)
56424.1	59.5	...	20.00(0.03)	19.61(0.01)	19.01(0.03)	18.55(0.01)	18.66(0.02)
56425.1	60.4	19.60(0.02)	19.04(0.04)	18.57(0.02)	18.69(0.02)
56428.2	63.4	...	20.03(0.02)	19.64(0.01)	19.06(0.02)	18.66(0.01)	18.82(0.02)
56435.1	70.0	...	19.97(0.07)	19.67(0.04)	19.17(0.04)	18.78(0.02)	18.98(0.03)
56438.2	73.0	...	20.24(0.11)	19.78(0.04)	19.25(0.04)	18.88(0.02)	19.17(0.03)
56445.0	79.6	...	20.28(0.03)	19.86(0.02)	19.36(0.03)	19.04(0.01)	19.30(0.02)
56448.1	82.5	...	20.32(0.03)	19.92(0.02)	19.42(0.03)	19.11(0.01)	19.35(0.02)

^aRest frame days relative to the time of *B*-band maximum given in Table 2.

Table A3. CSP natural system photometry for CSS140126.

MJD	Phase ^a	<i>B</i>	<i>g</i>	<i>V</i>	<i>r</i>	<i>i</i>	<i>Y</i>	<i>J</i>
Days	Days	Mag	Mag	Mag	Mag	Mag	Mag	Mag
56662.3	-5.3	18.50(0.01)	...	18.47(0.01)	18.58(0.01)	18.86(0.02)
56663.3	-4.3	18.43(0.01)	...	18.42(0.01)	18.51(0.01)	18.83(0.02)
56664.3	-3.4	18.36(0.01)	...	18.35(0.01)	18.45(0.01)	18.79(0.02)
56665.3	-2.5	18.33(0.01)	...	18.29(0.01)	18.39(0.01)	18.75(0.02)
56666.4	-1.6	18.27(0.01)	...	18.25(0.01)	18.35(0.01)	18.77(0.01)	18.82(0.02)	18.76(0.02)
56667.3	-0.6	18.27(0.01)	...	18.26(0.01)	18.32(0.01)	18.73(0.01)
56668.3	0.3	18.30(0.01)	...	18.25(0.01)	18.29(0.01)	18.68(0.01)
56669.3	1.2	18.86(0.02)	18.81(0.02)
56670.3	2.2	18.32(0.01)	...	18.28(0.01)	18.26(0.01)	18.64(0.01)
56671.3	3.1	18.86(0.02)	18.89(0.02)
56672.3	4.0	18.39(0.02)	...	18.28(0.02)	18.23(0.01)	18.60(0.02)
56675.3	6.8	19.00(0.03)	19.19(0.04)
56680.4	11.5	18.72(0.02)	...	18.43(0.02)
56681.3	12.4	18.82(0.02)	...	18.50(0.01)	18.46(0.01)	19.16(0.02)
56684.4	15.2	19.15(0.01)	...	18.68(0.01)	18.64(0.01)	19.28(0.02)
56691.2	21.6	20.11(0.02)	19.73(0.01)	19.24(0.01)	...	19.20(0.02)
56692.3	22.6	20.26(0.02)	...	19.32(0.01)	18.96(0.01)	19.15(0.02)
56693.3	23.5	19.00(0.02)	19.13(0.02)
56694.3	24.4	20.48(0.03)	19.06(0.01)	19.16(0.02)
56695.3	25.4	19.09(0.02)	19.15(0.02)
56696.3	26.3	19.17(0.01)	19.13(0.02)
56697.3	27.2	19.20(0.01)	19.15(0.02)
56698.3	28.1	19.24(0.01)	19.22(0.02)
56699.4	29.2	19.91(0.02)	19.30(0.02)
56708.3	37.4	20.11(0.04)	19.61(0.03)	19.55(0.03)
56709.4	38.5	20.21(0.04)	19.69(0.02)	19.59(0.02)
56710.4	39.3	20.26(0.04)	19.72(0.02)	19.67(0.03)
56711.4	40.3	20.28(0.04)	19.78(0.02)	19.69(0.02)
56712.4	41.2	20.30(0.03)	19.79(0.02)	19.76(0.03)
56713.4	42.2	20.39(0.03)	19.81(0.02)	19.82(0.03)

^aRest frame days relative to the time of *B*-band maximum given in Table 2.

Table A4. CSP natural system photometry for CSS140501.

MJD	Phase ^a	<i>B</i>	<i>V</i>	<i>r</i>	<i>i</i>	<i>Y</i>	<i>J</i>	<i>H</i>
Days	Days	Mag	Mag	Mag	Mag	Mag	Mag	Mag
56783.3	-3.6	18.42(0.02)	18.24(0.02)	18.22(0.02)	18.42(0.02)
56784.3	-2.7	18.39(0.01)	18.22(0.01)	18.22(0.01)	18.39(0.02)
56785.3	-1.8	18.38(0.01)	18.20(0.02)	18.18(0.01)	18.35(0.02)	18.28(0.01)	18.15(0.02)	...
56786.3	-0.8	18.34(0.01)	18.17(0.02)	18.18(0.02)	18.37(0.02)	18.26(0.01)	18.16(0.02)	18.24(0.04)
56787.3	0.1	18.22(0.01)	17.97(0.13)	...
56788.4	1.0	18.40(0.02)	18.13(0.02)	18.12(0.02)	18.28(0.04)
56789.2	1.9	18.40(0.02)	18.16(0.02)	18.10(0.01)	18.33(0.02)	18.39(0.02)	18.21(0.02)	...
56790.2	2.8	18.43(0.03)	18.17(0.02)	18.11(0.02)	18.36(0.02)
56791.2	3.8	18.49(0.04)	18.16(0.03)	18.11(0.02)	18.33(0.02)	18.27(0.01)	18.26(0.02)	18.31(0.04)
56792.3	4.7	18.51(0.04)	18.12(0.03)	18.10(0.02)	18.39(0.03)
56793.2	5.6	18.57(0.03)	18.20(0.03)	18.12(0.02)	18.35(0.02)	18.30(0.02)	18.34(0.02)	18.21(0.04)
56794.3	6.6	18.63(0.03)	18.25(0.02)	18.10(0.02)	18.36(0.02)
56795.3	7.5	18.65(0.02)	18.27(0.02)	18.13(0.02)	18.36(0.02)
56796.2	8.4	18.77(0.02)	18.28(0.02)	18.19(0.02)	18.40(0.02)
56798.3	10.3	18.93(0.04)	18.38(0.02)	18.24(0.02)	18.39(0.04)
56804.2	15.8	19.73(0.02)	18.82(0.01)	18.44(0.01)	18.54(0.01)
56808.3	19.5	20.14(0.02)	19.10(0.02)	18.64(0.01)	18.59(0.01)
56810.3	21.4	20.35(0.02)	19.24(0.01)	18.74(0.01)	18.63(0.02)

^aRest frame days relative to the time of *B*-band maximum given in Table 2.

Table A5. CSP natural system photometry for SN 2015M.

MJD	Phase ^a	<i>u</i>	<i>B</i>	<i>g</i>	<i>V</i>	<i>r</i>	<i>i</i>	<i>Y</i>	<i>J</i>	<i>H</i>
Days	Days	Mag	Mag	Mag	Mag	Mag	Mag	Mag	Mag	Mag
57154.1	-14.1	...	17.59(0.02)	...	17.40(0.02)	17.51(0.02)	17.81(0.03)
57155.1	-13.1	17.58(0.04)	17.22(0.01)	17.10(0.01)	17.05(0.01)	17.16(0.01)	17.46(0.02)
57156.1	-12.1	17.18(0.02)	16.86(0.01)	16.75(0.01)	16.73(0.01)	16.82(0.01)	17.12(0.02)
57157.1	-11.1	16.92(0.02)	16.56(0.01)	16.48(0.01)	16.47(0.01)	16.59(0.01)	16.93(0.04)
57158.1	-10.2	16.66(0.01)	16.33(0.01)	16.24(0.01)	16.26(0.01)	16.38(0.01)	16.70(0.01)
57159.1	-9.2	16.51(0.02)	16.13(0.01)	16.07(0.01)	16.09(0.01)	16.20(0.01)	16.51(0.01)
57160.1	-8.2	16.33(0.01)	15.97(0.01)	15.91(0.01)	15.95(0.01)	16.06(0.01)	16.40(0.01)
57161.1	-7.2	16.20(0.01)	...	15.78(0.01)	15.84(0.01)	15.94(0.01)	16.28(0.01)
57162.1	-6.3	16.12(0.01)	15.75(0.01)	15.68(0.00)	15.74(0.01)	15.85(0.01)	16.23(0.01)
57163.1	-5.3	16.09(0.01)	15.67(0.01)	15.61(0.00)	15.65(0.01)	15.77(0.01)	16.17(0.01)
57164.1	-4.3	16.07(0.01)	15.61(0.01)	15.55(0.01)	15.58(0.01)	15.71(0.01)	16.13(0.01)
57165.1	-3.3	...	15.59(0.01)	15.51(0.00)	15.55(0.01)	15.65(0.01)	16.06(0.09)
57166.1	-2.3	16.05(0.01)	15.56(0.00)	15.48(0.00)	15.52(0.01)	15.61(0.00)	16.10(0.01)
57169.1	0.6	16.16(0.04)	15.90(0.03)	16.30(0.03)
57170.1	1.6	16.22(0.04)	15.98(0.03)	16.28(0.03)
57172.1	3.5	16.30(0.05)	16.10(0.03)	16.32(0.04)
57173.1	4.5	16.43(0.02)	15.67(0.01)	15.53(0.01)	15.45(0.01)	15.52(0.01)	16.07(0.02)	16.34(0.04)	16.04(0.03)	16.38(0.04)
57174.1	5.5	16.48(0.02)	15.74(0.01)	15.58(0.01)	15.50(0.01)	15.55(0.01)	16.17(0.01)
57175.1	6.5	16.59(0.03)	15.76(0.01)	15.62(0.01)	15.52(0.01)	15.61(0.01)	16.22(0.01)
57176.1	7.4	16.65(0.02)	15.82(0.01)	15.66(0.01)	15.57(0.01)	15.60(0.01)	16.23(0.01)
57177.1	8.4	16.75(0.02)	15.89(0.01)	15.72(0.01)	15.58(0.01)	15.66(0.01)	16.28(0.01)
57178.1	9.4	16.82(0.02)	15.95(0.01)	15.78(0.01)	15.63(0.01)	15.70(0.01)	16.30(0.01)
57179.0	10.3	16.92(0.02)	16.04(0.01)	15.84(0.00)	15.69(0.01)	15.74(0.01)	16.35(0.01)
57180.1	11.3	17.02(0.02)	16.13(0.01)	15.92(0.01)	15.74(0.01)	15.79(0.00)	16.39(0.01)
57181.0	12.2	17.18(0.02)	16.21(0.01)	15.99(0.00)	15.81(0.01)	15.84(0.01)	16.43(0.01)
57182.0	13.2	17.30(0.02)	16.32(0.01)	16.09(0.00)	15.87(0.01)	15.88(0.00)	16.47(0.01)
57184.0	15.2	17.55(0.02)	16.52(0.01)	16.27(0.01)	16.01(0.01)	15.96(0.01)	16.48(0.01)

^aRest frame days relative to the time of *B*-band maximum given in Table 2.

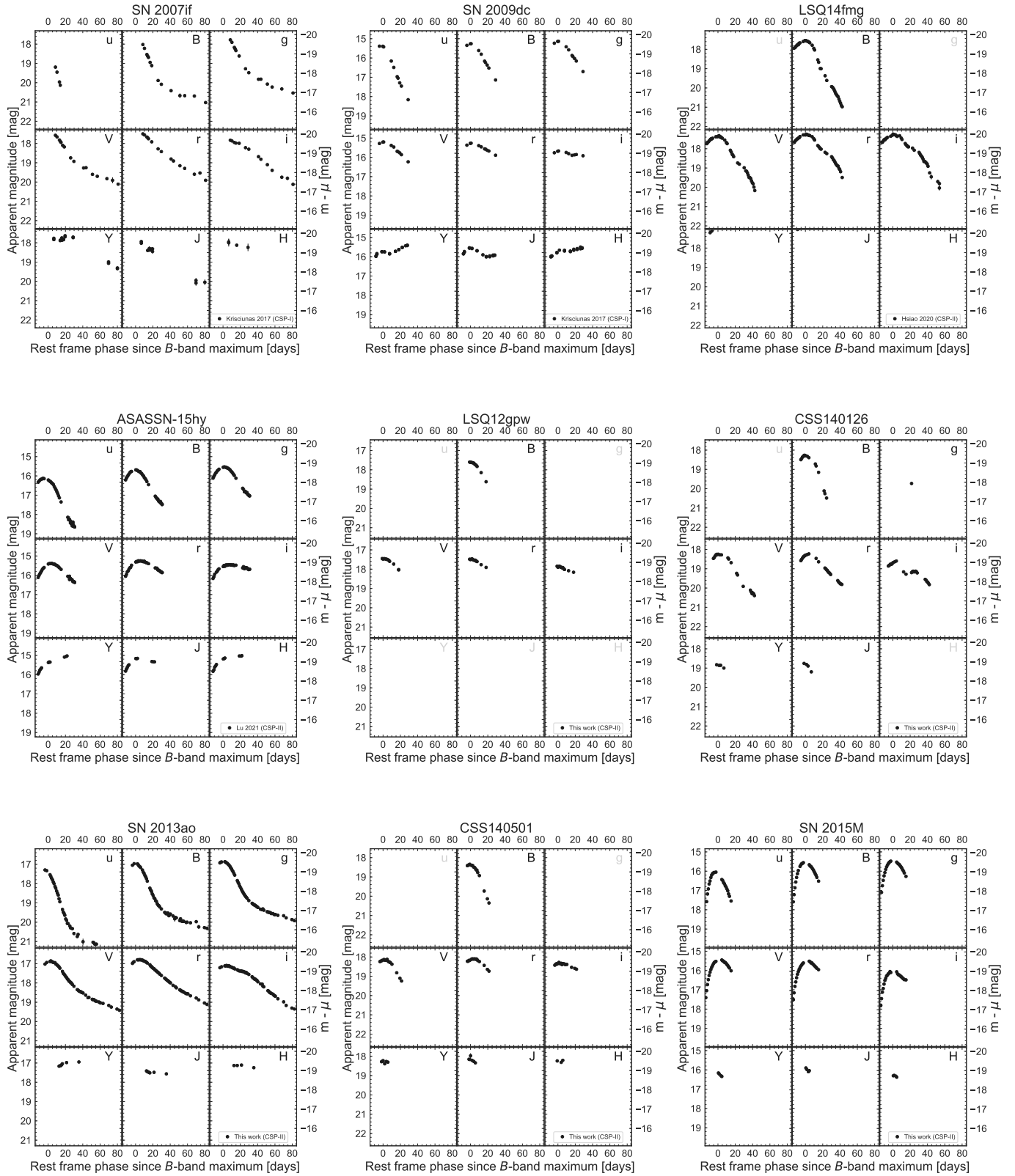


Figure A1. Individual light curves of the nine 2003fg-like SNe followed by the CSP. If the data were previously published elsewhere it is stated in the figure caption.

Table A6. Journal of Spectroscopic Observations.

SN	JD−2450000 (Days)	Phase ^a (Days)	Telescope	Instrument
Optical				
2007if	4355.86	+5.48	du Pont	B & C
2007if	4361.83	+11.04	du Pont	B & C
2007if	4365.83	+14.77	Clay	LDSS3
2007if	4377.69	+25.81	ESO 3.6m	EFOSC2
2007if	4381.67	+29.51	Baade	IMACS
2009dc	4938.82	−8.08	Clay	LDSS3
2009dc	4939.79	−7.13	du Pont	B & C
2009dc	4943.78	−3.22	du Pont	B & C
2009dc	4944.80	−2.22	du Pont	B & C
2009dc	4951.75	+4.58	Clay	LDSS3
2009dc	4952.80	+5.61	Clay	LDSS3
2009dc	4965.69	+18.23	Baade	IMACS
2009dc	4974.70	+27.05	du Pont	B & C
2009dc	4982.65	+34.83	du Pont	B & C
LSQ12gpw	6275.44	+5.42	NOT	ALFOSC
2013ao	6388.48	+8.67	NOT	ALFOSC
2013ao	6388.48	+24.87	SALT	RSS
2013ao	6407.50	+43.10	NOT	ALFOSC
CSS140501 ^b	6798.64	−0.08	NOT	ALFOSC
2015M	7158.62	−10.15	NOT	ALFOSC
2015M	7166.42	−2.52	NOT	ALFOSC
2015M	7176.45	+7.28	NOT	ALFOSC
2015M	7180.40	+11.14	NOT	ALFOSC
2015M	7191.50	+21.99	NOT	ALFOSC
NIR				
2013ao	6371.14	+8.74	Baade	FIRE
2013ao	6376.22	+13.03	Baade	FIRE
2013ao	6383.18	+19.66	Baade	FIRE
2013ao	6385.28	+21.66	Baade	FIRE
2013ao	6431.15	+65.32	Baade	FIRE
2015M	7175.52	+6.37	Baade	FIRE

^aRest frame days relative to the time of *B*-band maximum given in Table 2.

^bCSS140501-170414+174839.

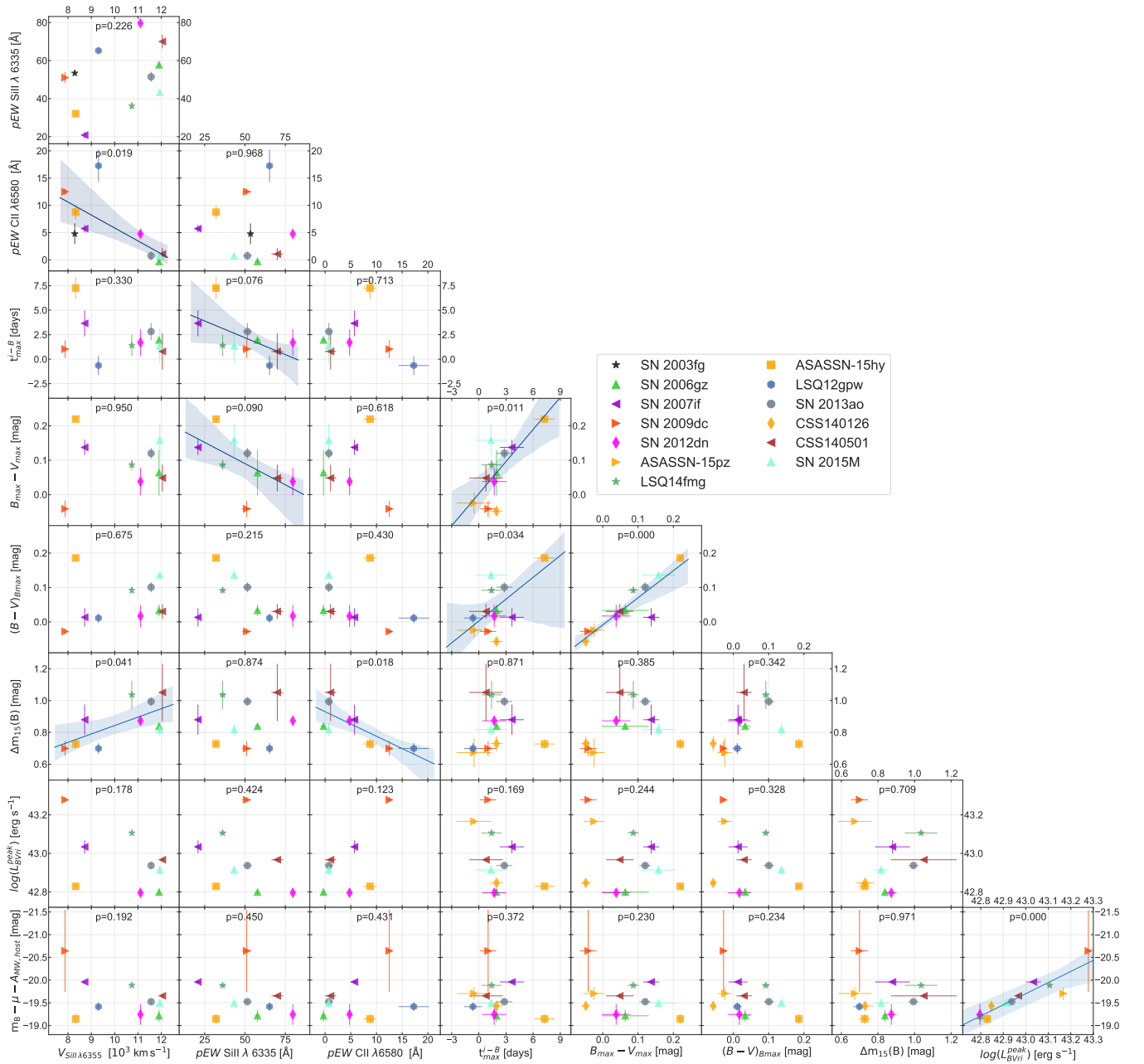


Figure B1. A pair-plot of measured parameters of 2003fg-like SNe, on top of each panel the p-value is given. Potentially significant correlations with $p \leq 0.1$ are presented by a best-fit line determined by a least square technique along with 95% confidence intervals in each panel.